AMAS COURSE ON RANDOM MATERIAL MICROSTRUCTURES
RMM'04 – (PP.101–153) – WARSAW, FEBRUARY 2-4, 2004

Micromechanics of random heterogeneous materials

S. C. BAXTER

University of South Carolina
Department of Mechanical Engineering
Columbia, SC 29208
baxter@sc.edu

The following article contains notes for 4 lectures. The lectures are first, an overview of classical micromechanics, assumptions, theoretical formulations and definitions, and well-known models. The second lecture discusses some directions and applications that the stochastic community has taken toward developing stochastic micromechanics. The third lecture presents the background and highlights of work done by this author and Dr. Lori Graham-Brady, of the Johns Hopkins University Department of Civil Engineering, in developing the methodology of moving window micromechanics. The fourth lecture presents the very beginnings of experimental work, initiated with Dr. Stephen McNeill, of the University of South Carolina Department of Mechanical Engineering, that we hope will help verify, and extend the moving window approach.

Key words: *classical micromechanics, stochastic micromechanics, moving window approximations, computational mechanics.*

1. Classical micromechanics

1.1. The basics of linear elasticity

For infinitesimal deformations, the total strain is the sum of the elastic strain and what can generally be referred to as eigenstrains, ε^*_{ij},

$$\varepsilon_{ij} = \varepsilon^E_{ij} + \varepsilon^*_{ij}, \tag{1.1}$$

where the total (linear) strain, $\boldsymbol{\varepsilon}$, defined in terms of the displacements, $\mathbf{u}$, is

$$\varepsilon_{ij} = \frac{1}{2}\left(u_{i,j} + u_{j,i}\right). \tag{1.2}$$

Solving for the elastic strains, ε_{ij}^E, and using Hooke's Law (generalized) for an elastic material

$$\sigma_{ij} = C_{ijkl}\varepsilon_{kl}^E = C_{ijkl}\left(\varepsilon_{kl} - \varepsilon_{kl}^*\right), \tag{1.3}$$

where σ_{ij}, ε_{ij} are the stress and total strain components, respectively, and C_{ijkl} is the elastic stiffness tensor. The inverse relationship also holds,

$$\varepsilon_{ij}^E = S_{ijkl}\sigma_{kl}, \tag{1.4}$$

where S_{ijkl} is the elastic compliance tensor. Both tensors displays major and minor symmetries, e.g.,

$$C_{ijkl} = C_{klij}, \qquad C_{ijkl} = C_{ijlk}. \tag{1.5}$$

This allows the constitutive law of an isotropic material can be written as

$$\sigma_{ij} = 2\mu\varepsilon_{ij}^E + \lambda\delta_{ij}\varepsilon_{kk}^E, \tag{1.6}$$

where λ and μ are the Lamé constants and δ_{ij} is the Kronecker delta and the summation convention for repeated indices is employed.

The engineering constants, E, the Young's modulus, ν, the Poisson's ratio and K, the bulk modulus are related to the Lamé constants by

$$E = \frac{\mu(3\lambda + 2\mu)}{(\lambda + \mu)}, \qquad \nu = \frac{\lambda}{2(\lambda + \mu)}, \qquad K = \lambda + \frac{2\mu}{3}. \tag{1.7}$$

The equilibrium equations, in the absence of body forces, are

$$\sigma_{ij,j} = 0, \quad i = 1, 2, 3, \tag{1.8}$$

and boundary condition for external surfaces that are free of forces are

$$\sigma_{ij}n_j = 0, \quad i = 1, 2, 3, \tag{1.9}$$

where the n_j are the components of an external, outward unit, normal vector on the boundary.

1.2. Fundamental concepts

1.2.1. Representative Volume Element (RVE). An RVE is a sample of the material that is structurally and statistically representative of the entire material – on average. It must be large by comparison with the scale of the microstructure, i.e., it contains a large view of the microstructure, but it is only useful it if is also much smaller than the bulk material. As such, an RVE exhibits the properties of the composite medium and these properties can be shown to be relatively insensitive to macroscopically uniform boundary conditions. In other words, they fluctuate about a mean with a wavelength small compared to the dimensions of the volume. The idea is that one can then perform analysis on the RVE rather than the full sample.

1.2.2. Volume averaging. When the macro conditions of homogeneous stress or homogeneous strain are imposed on an RVE, with volume V,the average stress and average strain can be defined as:

$$\bar{\sigma}_{ij} = \frac{1}{V}\int_V \sigma_{ij}\, dV, \tag{1.10}$$

$$\bar{\varepsilon}_{ij} = \frac{1}{V}\int_V \varepsilon_{ij}\, dV. \tag{1.11}$$

1.2.3. Homogeneous boundary conditions. A homogeneous strain field can be produced by applying displacements on the boundary S

$$u_i(S) = \varepsilon^0_{ij} x_j \tag{1.12}$$

where the ε^0_{ij} are constant strains. Similarly, a homogeneous stress field is produced by applying tractions, t_i on the boundary S

$$t_i(S) = \sigma^0_{ij} n_j \tag{1.13}$$

where the σ^0_{ij} are constant stresses and the n_j are the components of the outward unit normal vector.

1.2.4. Average Strain Theorem. Consider a two phase RVE where homogeneous strains are applied to the boundary. Using the definition of strain, the average strain is

$$2V\bar{\varepsilon}_{ij} = \int_{V_1} (u^{(1)}_{i,j} + u^{(1)}_{j,i})\, dV + \int_{V_2} (u^{(2)}_{i,j} + u^{(2)}_{j,i})\, dV. \tag{1.14}$$

Gauss' theorem

$$\int_V u_{i,q}\, dV = \int_{\partial V} u_i n_q\, dV, \tag{1.15}$$

when used in the average strain Eq. (1.14), results in

$$2V\bar{\varepsilon}_{ij} = \int_{S_1} (u^{(1)}_i n_j + u^{(1)}_j n_i)\, dS + \int_{S_2} (u^{(2)}_i n_j + u^{(2)}_j n_i)\, dS \tag{1.16}$$

where S_1, S_2 are the phase boundaries. On S_{12}, the interface boundary, assuming perfect bonding, the contributions to the integrals from S_{12} cancel, leaving

$$\bar{\varepsilon}_{ij} = \frac{1}{2V}\int_S (u_i n_j + u_j n_i)\, dS. \tag{1.17}$$

Substituting Eq. (1.17) into the equations for homogeneous boundary conditions, Eq. (1.12), results in the statement of the *Average Strain Theorem*,

$$\bar{\varepsilon}_{ij} = \varepsilon^0_{ij}. \tag{1.18}$$

The average strains in the composite RVE are the same as the constant strains applied on the boundary.

1.2.5. Average Stress Theorem. Again, consider a two phase RVE, this time with homogeneous stresses applied to the boundary S. Equilibrium, in the absence of body forces, implies

$$\sigma_{ij,j} = 0,$$

and with the definition,

$$\frac{\partial x_i}{\partial x_j} = \delta_{ij}$$

it can be established that

$$\sigma_{ij} = \sigma_{ik}\delta_{kj} = \sigma_{ik}\delta_{jk} = \left(\sigma_{ik}\frac{\partial x_j}{\partial x_k}\right) \quad \text{and} \quad \left(\sigma_{ik}x_j\right),_k = \sigma_{ik,k}x_j + \sigma_{ik}\frac{\partial x_j}{\partial x_k}.$$

Since

$$\sigma_{ij,j} = 0 \quad \Rightarrow \quad \sigma_{ik,k}x_j = 0 \tag{1.19}$$

thus,

$$\sigma_{ij} = \left(\sigma_{ik}x_j\right),_k. \tag{1.20}$$

Using Eq. (1.2), the definition of average stress,

$$\bar{\sigma}_{ij} = \frac{1}{V}\int_V \left(\sigma_{ik}x_j\right),_k \, dV \tag{1.21}$$

and Gauss' Theorem yields

$$V\bar{\sigma}_{ij} = \int_{S_1} \sigma^{(1)}_{ik}x_j n^{(1)}_k dS + \int_{S_2} \sigma^{(2)}_{ik}x_j n^{(2)}_k dS. \tag{1.22}$$

Since the tractions are continuous at the interface, i.e.,

$$\sigma^{(1)}_{ij}n^{(1)}_j = -\sigma^{(2)}_{ij}n^{(2)}_j \quad \text{on} \quad S_{12}, \tag{1.23}$$

those parts of the integral cancel and

$$V\bar{\sigma}_{ij} = \int_S \sigma_{ik}x_j n_k \, dS = \sigma^0_{ij}\int_S x_j n_k \, dS = \sigma^0_{ij}\int_V x_{j,k} \, dV \quad \Rightarrow \quad \bar{\sigma}_{ij} = \sigma^0_{ij}. \tag{1.24}$$

The *Average Stress Theorem* states that the average stresses in the composite are the same as the constant stresses applied on the boundary.

1.2.6. Effective Elastic Moduli. Homogeneous displacement boundary conditions produce uniform strains in homogeneous materials. Applying these conditions to an RVE and using the average strain theorem implies that these are also the average strains in the composite.

$$\varepsilon^0_{ij} = \bar{\varepsilon}_{ij}. \tag{1.25}$$

If a displacement field generated by $\varepsilon^0_{kl} = 1$ is designated by $u_i^{(kl)}(x)$ then the displacement field can be written, using superposition, as

$$u_i(x) = \varepsilon^0_{kl} u_i^{(kl)}(x), \tag{1.26}$$

where there is a summation over k and l. The resulting strain is then given by

$$\varepsilon_{ij}(x) = \frac{1}{2}\varepsilon^0_{kl}(u^{(kl)}_{i,j} + u^{(kl)}_{j,i}). \tag{1.27}$$

The resulting stress at a point x is

$$\sigma_{ij}(x) = \frac{1}{2}C_{ijpq}(x)\varepsilon^0_{kl}(u^{(kl)}_{p,q} + u^{(kl)}_{q,p}), \tag{1.28}$$

with

$$C_{ijkl} = C^{(1)}_{ijkl}, \quad \text{or} \quad C^{(2)}_{ijkl}. \tag{1.29}$$

Using the definition of average stress it can be shown that

$$\bar{\sigma}_{ij}(x) = C^*_{ijkl}\bar{\varepsilon}_{kl}, \tag{1.30}$$

where

$$C^*_{ijkl} = \frac{1}{2V}\int_V C_{ijpq}(x)\left(u^{(kl)}_{p,q} + u^{(kl)}_{q,p}\right) dV. \tag{1.31}$$

Thus the average stress is related to the average strain through *effective* elastic moduli. A similar argument can be used to construct effective compliances.

1.2.7. Relationships between the averages. For a two phase composite, (c_1 and c_2 are volume fractions, $c_1 + c_2 = 1$), with perfect bonding

$$\bar{\sigma}_{ij} = c_1\bar{\sigma}^{(1)}_{ij} + c_2\bar{\sigma}^{(2)}_{ij} \tag{1.32}$$

and

$$\bar{\varepsilon}_{ij} = c_1\bar{\varepsilon}^{(1)}_{ij} + c_2\bar{\varepsilon}^{(2)}_{ij}. \tag{1.33}$$

Therefore,

$$\begin{aligned}\bar{\sigma}_{ij}(x) &= C^*_{ijkl}\bar{\varepsilon}_{kl} \\ &= C^*_{ijkl}\varepsilon^0_{kl},\end{aligned}$$

$$C^*_{ijkl}\varepsilon^0_{kl} = c_1\bar{\sigma}^{(1)}_{ij} + c_2\bar{\sigma}^{(2)}_{ij},$$

$$C^*_{ijkl}\varepsilon^0_{kl} = c_1 C^{(1)}_{ijkl}\bar{\varepsilon}^{(1)}_{kl} + c_2 C^{(2)}_{ijkl}\bar{\varepsilon}^{(2)}_{kl}. \tag{1.34}$$

With

$$c_1\bar{\varepsilon}^{(1)}_{ij} = \bar{\varepsilon}_{ij} - c_2\bar{\varepsilon}^{(2)}_{ij}, \qquad \bar{\varepsilon}_{ij} = \varepsilon^0_{ij}, \tag{1.35}$$

$$C^*_{ijkl}\varepsilon^0_{kl} = C^{(1)}_{ijkl}\varepsilon^0_{kl} + c_2\left(C^{(2)}_{ijkl} - C^{(1)}_{ijkl}\right)\bar{\varepsilon}^{(2)}_{kl} \tag{1.36}$$

and

$$\frac{\bar{\varepsilon}^{(2)}_{kl}}{\varepsilon^0_{kl}} = \frac{C^*_{ijkl} - C^{(1)}_{ijkl}}{c_2\left(C^{(2)}_{ijkl} - C^{(1)}_{ijkl}\right)}. \tag{1.37}$$

The effective moduli can be determined provided the strain in the second phase is known.

1.2.8. Concentration matrices. In a two phase composite where, $\bar{\sigma} = c_1\bar{\sigma}^{(1)} + c_2\bar{\sigma}^{(2)}$, and $\bar{\sigma}^{(i)} = C^{(i)}\bar{\varepsilon}^{(i)}$, then

$$\bar{\sigma} = c_1 C^{(1)}_1\bar{\varepsilon}^{(1)} + c_2 C^{(2)}\bar{\varepsilon}^{(2)}. \tag{1.38}$$

The relationship between the average strains in a phase and the overall strain in the composite can be expressed as

$$\bar{\varepsilon}^{(1)} = A_1\bar{\varepsilon}, \quad \bar{\varepsilon}^{(2)} = A_2\bar{\varepsilon}, \quad \text{and for example} \quad \left[\frac{\bar{\varepsilon}^{(2)}}{\bar{\varepsilon}} = \frac{\bar{\varepsilon}^{(2)}}{\varepsilon^0} = A_2\right]. \tag{1.39}$$

$A_1$and A_2 are called strain concentration matrices and $I = c_1A_1 + c_2A_2$, where I is the identity matrix. In this case the effective stiffness tensor can be written as

$$C^* = c_1C^{(1)}A_1 + c_2C^{(2)}A_2. \tag{1.40}$$

See Aboudi (1991), Nemat-Nasser and Hori (1999) for more details.

1.3. Classic models in micromechanics

1.3.1. Voigt approximation. The Voigt approximation (Voigt 1889) is one of the simplest models used to evaluate the effective properties of a composite; it was originally introduced to estimate the average constants of polycrystals. It is assumed that the strain throughout the bulk material is uniform (iso-strain).

This implies that $A_1 = A_2 = I$ and so

$$C^* = c_1 C^{(1)} + c_2 C^{(2)}. \tag{1.41}$$

When used to describe individual properties, for example the Young's modulus, this is known as the Rule of Mixtures.

1.3.2. Reuss approximation. The inverse assumption to Voigt is the Reuss Approximation (Reuss 1929) which assumes that the stress is uniform (iso-stress) throughout the phases. This implies

$$S^* = c_1 S^{(1)} + c_2 S^{(2)}. \tag{1.42}$$

where S^* is the effective compliance tensor. Neither Voigt nor Reuss are correct. Under the Voigt model the implied tractions across the boundaries of the phases would, in general violate equilibrium, and under the Reuss model the resulting strains would force debonding of the phases. Hill (1952) proved that the actual moduli lie somewhere between these two approximations, regardless of geometry.

1.3.3. Hashin–Shtrikman. Using variational principles, in Hashin (1962) and Hashin–Shtrikman (1963), bounds are established on materials that could be considered "mechanical mixtures of a number of different isotropic and homogeneous elastic phases" and regarded as statistically isotropic and homogeneous. Using this method, and specializing to a two phase material, the bounds, (upper (K_2^*) and lower (K_1^*), e.g.) on the effective bulk and shear moduli bounds were found as

$$K_1^* = K_1 + \frac{c_2}{\dfrac{1}{K_2 - K_1} + \dfrac{3c_1}{3K_1 + 4G_1}}, \tag{1.43}$$

$$G_1^* = G_1 + \frac{c_2}{\dfrac{1}{G_2 - G_1} + \dfrac{6(K_1 + 2G_1)c_1}{5G_1(3K_1 + 4G_1)}}, \tag{1.44}$$

$$K_2^* = K_2 + \frac{c_1}{\dfrac{1}{K_1 - K_2} + \dfrac{3c_2}{3K_2 + 4G_2}}, \tag{1.45}$$

$$G_1^* = G_2 + \frac{c_1}{\dfrac{1}{G_1 - G_2} + \dfrac{6(K_2 + 2G_2)c_2}{5G_2(3K_2 + 4G_2)}}, \tag{1.46}$$

where $K_2 > K_1$, $G_2 > G_1$, $c_1 + c_2 = 1$. The bounds are exact if $K_1 \neq K_2$, $G_1 = G_2$.

1.3.4. The dilute approximation. The dilute approximation can be used to model a dilute suspension of spherical elastic particles in a continuous elastic phase. The interaction between particles is neglected. The problem reduces to that of solving the problem of a spherical inclusion in an infinite matrix subjected to hydrostatic loading at infinity. Under the assumption of spherical symmetry, $u_r = u_r(r)$, $u_\phi = 0$, $u_\vartheta = 0$, the equilibrium condition reduces to

$$\frac{\partial^2}{\partial r^2}u_r + \frac{2}{r}\frac{\partial}{\partial r}u_r - \frac{2}{r^2}u_r = 0, \qquad \underset{r\to\infty}{u} = \varepsilon_{kk}^0. \tag{1.47}$$

The general solution is

$$u_r^{(1)} = Cr, \tag{1.48}$$

in the particle, and

$$u_r^{(2)} = Ar + \frac{B}{r^2} \tag{1.49}$$

in the matrix.

With the interfacial continuity conditions

$$u_r^{(1)}(a) = u_r^{(2)}(a), \qquad \sigma_{rr}^{(1)}(a) = \sigma_{rr}^{(2)}(a), \tag{1.50}$$

one can solve for the ratio between the strains in the second phase and the applied strain

$$\frac{\bar{\varepsilon}_{kk}^{(2)}}{\varepsilon_{kk}^0} = \frac{3C}{3A} = \frac{3(\lambda_1 + 2\mu_1)}{3\lambda_2 + 2\mu_2 + 4\mu_1}. \tag{1.51}$$

Using the relationship between averages, Eq. (1.37), the effective bulk modulus is then

$$K^* = K_1 + \frac{c_2(K_2 + K_1)(3K_1 + 4\mu_1)}{3K_2 + 4\mu_1}. \tag{1.52}$$

Solving the problem of a homogenous medium in a state of simple shear results in

$$\frac{\bar{\varepsilon}_{12}^{(2)}}{\varepsilon_{12}^0} = \frac{15(1 - \nu_1)}{\mu_1(7 - 5\nu_1) + 2(4 - 5\nu_1)\mu_2}. \tag{1.53}$$

Again, using the relationship between averages, Eq. (1.37),

$$\frac{\mu^*}{\mu_1} = 1 - \frac{15(1 - \nu_1)\left(1 - \frac{\mu_2}{\mu_1}\right)c_2}{(7 - 5\nu_1) + 2(4 - 5\nu_1)\frac{\mu_2}{\mu_1}} \tag{1.54}$$

and for $\nu_1 = 0.5$,

$$\frac{\mu^*}{\mu_1} = 1 - \frac{5c_2}{2}. \tag{1.55}$$

1.3.5. Eshelby's equivalent inclusion. Eshelby (1957, 1959, 1961) considered the problem of an ellipsoidal inclusion in an infinite isotropic matrix. He defined an inclusion as a region of the matrix that has the same elastic properties as the bulk material but which undergoes what would be a stress-free transformation – if it were not surrounded by the rest of the matrix. Since it *is* surrounded, the transformation produces strains – eigenstrains – in the inclusion. What Eshelby realized was that this problem, with macro boundary conditions, should be equivalent to the problem of a region in a matrix with different material properties, and inhomogeneity, same boundary conditions. In one case an inhomogeneity in the strain field would be due to the transformation strains, and in the other due to the different constitutive properties.

He formally considered the two problems of inhomogeneity: the disturbance in an applied stress field is due to either (1) an ellipsoidal inhomogeneity, where an ellipsoidal domain has elastic properties different from the matrix or (2) an ellipsoidal inclusion, (same region as the inhomogeneity above) with identical elastic properties as the matrix, but with an eigenstrain.

Problem 1:

We consider an inhomogeneity Ω (properties $\hat{C}_{ijkl}$) in domain D (properties C_{ijkl}). An applied stress (at infinity) results in the following strain

$$\sigma^0_{ij}, \quad \varepsilon^0_{ij} = \frac{1}{2}(u^0_{i,j} + u^0_{j,i}). \tag{1.56}$$

Denoting the stress and elastic strain due to the inhomogeneities, (with no superscripts),

$$\sigma_{ij}, \quad \varepsilon_{ij} = \frac{1}{2}(u_{i,j} + u_{j,i}). \tag{1.57}$$

the total stress and total displacement for the problem would be

$$\sigma^0_{ij} + \sigma_{ij}, \quad u^0_i + u_i. \tag{1.58}$$

The disturbance stresses satisfy equilibrium and

$$\sigma_{ij,j} = 0, \quad \underset{x\to\infty}{\sigma_{ij}} = 0, \quad \sigma_{ij}n_j = 0. \tag{1.59}$$

Using Hooke's Law, we then have

$$\sigma^0_{ij} + \sigma_{ij} = \hat{C}_{ijkl}\left(u^0_{k,l} + u_{k,l}\right) \quad \text{in} \quad \Omega \tag{1.60}$$

and

$$\sigma^0_{ij} + \sigma_{ij} = C_{ijkl}\left(u^0_{k,l} + u_{k,l}\right) \quad \text{in} \quad D - \Omega. \tag{1.61}$$

Problem 2:

We consider an inclusion Ω, (properties C_{ijkl}) in domain D (properties C_{ijkl}) with an equivalent eigenstrain ε^*_{ij} and an applied strain at infinity ε^0_{ij}, in this case,

$$\sigma^0_{ij} + \sigma_{ij} = C_{ijkl}\left(u^0_{k,l} + u_{k,l} - \varepsilon^*_{kl}\right) \quad \text{in} \quad \Omega, \tag{1.62}$$

$$\sigma^0_{ij} + \sigma_{ij} = C_{ijkl}\left(u^0_{k,l} + u_{k,l}\right) \quad \text{in} \quad D - \Omega. \tag{1.63}$$

The necessary and sufficient condition for these two problems to be equivalent is the equivalence of Eqs. (1.60) and (1.62) thus

$$\hat{C}_{ijkl}\left(u^0_{k,l} + u_{k,l}\right) = C_{ijkl}\left(u^0_{k,l} + u_{k,l} - \varepsilon^*_{kl}\right) \quad \text{in} \quad \Omega \tag{1.64a}$$

or

$$\hat{C}_{ijkl}\left(\varepsilon^0_{kl} + \varepsilon_{kl}\right) = C_{ijkl}\left(\varepsilon^0_{kl} + \varepsilon_{kl} - \varepsilon^*_{kl}\right) \quad \text{in} \quad \Omega. \tag{1.64b}$$

Eshelby showed that, given ε^0, if the eigenstrains are uniform inside an ellipsoidal domain then the total strain $(\varepsilon^0_{ij} - \varepsilon_{ij})$ is uniform there too. Eshelby derived the elastic fields due to the inclusion and was able to explicitly solve for a concentration tensor, P_{ijkl}, known as Eshelby's tensor, for both isotropic and anisotropic materials, which relates the eigenstrains to the average strain in the body. Eshelby's tensor is symmetric with respect to the first two and last two indices, independent of the material properties of the included phase, defined by the aspect ratios of the ellipsoid and the properties of the matrix and depends only on the Poisson's ratio of the matrix and aspect ratios if the matrix is isotropic. (Mura (1987) has generated values for concentration tensors for shapes in addition to ellipses.) To use this method we consider a composite material loaded by a shear strain then, $\sigma^0_{12} = \bar{\sigma}$. The stress in the composite will vary, but can be written as $\sigma^0_{12} + \sigma_{12}$, where σ_{12} is the stress due to the inhomogeneity. Next consider a homogeneous material where the matrix and inclusions have the same elastic properties but the inclusions have eigenstrains. Ω_r is the r^{th} inclusion with the same volume and location as the r^{th} inhomogeneity. The two problem equivalency equation is then

$$2\mu\left(\varepsilon^0_{12} + \varepsilon_{12} - \varepsilon^*_{12}\right) = 2\hat{\mu}\left(\varepsilon^0_{12} + \varepsilon_{12}\right), \tag{1.65}$$

and μ, $\hat{\mu}$ are the shear modulus in the matrix and the inclusion, respectively.

The strain in the inclusion is

$$\bar{\varepsilon}^{(2)}_{12} = \varepsilon^0_{12} + \varepsilon_{12}. \tag{1.66}$$

Substituting Eq. (1.66) into the equivalency condition results in

$$\mu\left(\bar{\varepsilon}_{12}^{(2)} - \varepsilon_{12}^{*}\right) = \hat{\mu}\bar{\varepsilon}_{12}^{(2)}. \tag{1.67}$$

From Eshelby's work we have that

$$\varepsilon_{12} = 2P_{1212}\varepsilon_{12}^{*}, \qquad \sigma_{12} = 2\mu\varepsilon_{12}^{0}, \tag{1.68}$$

and, for spherical inclusions

$$P_{1212} = \frac{(4-5\nu)}{15(1-\nu)}, \tag{1.69}$$

where ν is the Poisson's ratio of the matrix.

Therefore,

$$\varepsilon_{12}^{*} = \frac{(\mu - \hat{\mu})\,\varepsilon_{12}^{0}}{\hat{m}} \tag{1.70}$$

where

$$\hat{m} = \mu + 2P_{1212}\,(\hat{\mu} - \mu)\,. \tag{1.71}$$

Then

$$A_2 = \frac{(\mu - \hat{\mu})}{\mu + 2P_{1212}\,(\hat{\mu} - \mu)} \tag{1.72}$$

and from Eq. (1.37) it follows that

$$\mu^{*} = \mu - c_2(\mu - \hat{\mu})A_2. \tag{1.73}$$

1.3.6. Self-Consistent Method. Eshelby assumed a well defined matrix. This is not always true, in polycrystalline materials a variety of properties can be exhibited but there is no clearly defined matrix phase. In these cases the interactions between particles (regions) is more significant. The self-consistent scheme again requires that the ratio in Eq. (1.37) be determined. In this case the factor is determined by assuming that a single particle reacts to an effective medium (rather than a homogeneous matrix). This, then, is the problem of an inclusion in a medium with unknown effective properties. The factors (shear and bulk) are then the same as for dilute but with effective properties replacing the properties of the matrix.

Thus,

$$\frac{\bar{\varepsilon}_{12}^{(2)}}{\bar{\varepsilon}_{12}^{0}} = \frac{15(1-\nu^{*})}{[\mu^{*}(7-5\nu^{*}) + 2(4-5\nu^{*})\mu_2]} \tag{1.74}$$

and

$$\frac{\bar{\varepsilon}_{kk}^{(2)}}{\bar{\varepsilon}_{kk}^{0}} = \frac{3(\lambda^{*} + 2\mu^{*})}{(3\lambda_2 + 2\mu_2 + 4\mu^{*})}. \tag{1.75}$$

Using equation (1.37)

$$\mu^* = \mu_1 + c_2(\mu_2 - \mu_1)\frac{15(1-\nu^*)}{[\mu^*(7-5\nu^*) + 2(4-5\nu^*)\mu_2]} \tag{1.76}$$

and

$$K^* = K_1 + c_2(K_2 - K_1)\frac{3\left(K^* + \frac{4}{3}\mu^*\right)}{3K_2 + 4\mu^*}. \tag{1.77}$$

Introduced by Hershey (1954) and Kröner (1958), the adaptation of this method for composites is often is often attributed to Hill (1965) and Budiansky (1965).

1.3.7. Generalized Self-Consistent Method. In this method, a single particle is embedded in a sheath of matrix which in turn is embedded in an effective medium. Solving the problem yields

$$\frac{\varepsilon_{kk}^{(2)}}{\varepsilon_{kk}^{0}} = \frac{\dfrac{(3K_1 + 4\mu_1)}{(3K_2 + 4\mu_1)}}{c_2\left[\dfrac{(3K_1 + 4\mu_1)}{(3K_2 + 4\mu_1)} - 1\right] + 1}. \tag{1.78}$$

With Eq. (1.37), this can be used to determine K^*.

To determine the effective shear modulus, the displacement field $u_x = cx$, $u_y = -cy$, $u_z = 0$ can be applied to the particle-sheath-matrix geometry and it can be shown that the effective shear modulus is governed by the quadratic equation

$$A\left(\frac{\mu^*}{\mu_1}\right)^2 + 2B\left(\frac{\mu^*}{\mu_1}\right) + C = 0, \tag{1.79}$$

and the constants A, B and C are functions of the inclusion and matrix elastic properties. This is significantly different from the self-consistent model in that the expression for μ^* is uncoupled from the effective bulk modulus K^*.

1.3.8. Differential scheme. Using this method a two phase composite is incrementally constructed from an initial known material as follows. Beginning with a two phase composite with volume V_0, a small volume ΔV is removed. This volume will include both phases. The removed volume is replaced by an equivalent volume of the second phase. Iteratively, at the $(i+1)^{\text{th}}$ step, the volume of phase 2, V_i, will be

$$V_{i+1} = V_0 c_i + \Delta V - \Delta V c_i \tag{1.80}$$

or

$$dc = (c_{i+1} - c_i) = \frac{\Delta V}{V_0}(1 - c_i). \tag{1.81}$$

Using Eq. (1.38) and the above yields

$$C^*(c_0 + \Delta c) = C^*(c) - \frac{\Delta V}{V_0}\left[C^{(2)} - C^*(c)\right] A_2 \tag{1.82}$$

or

$$\frac{dC^*}{dc} = \frac{1}{(1-c)}\left[C^{(2)} - C^*(c)\right] A_2 \tag{1.83}$$

where

$$C^* = C^{(1)}(0). \tag{1.84}$$

A_2 must be determined from the geometry and properties of the phases.

1.3.9. Mori–Tanaka (reformulated by Benveniste, 1987). The Mori–Tanaka method (Mori and Tanaka, 1973) was originally designed to calculate the average internal stress in the matrix of a material containing precipitates with eigenstrains. Benveniste (1987) reformulated it so that it could be applied to composite materials. He considered anisotropic phases and ellipsoidal phases. Using Eq. (1.36) and the idea of a concentration matrix we have that the effective properties can be defined as

$$C^* = C^{(1)} + c_2(C^{(2)} - C^{(1)})A_2, \qquad \bar{\varepsilon}^{(2)} = A_2\varepsilon^0. \tag{1.85}$$

We refer to the concentration tensor, from the dilute approximation, as

$$A_2 \equiv T \tag{1.86}$$

where T can be written in terms of Eshelby's tensor, P, as

$$T = \left[I + P\left[C^{(1)}\right]^{-1}\left(C^{(2)} - C^{(1)}\right)\right]^{-1}, \tag{1.87}$$

and I is the fourth order identity tensor. This approximation, due to the dilute model, neglects particle interactions and so is most valid at dilute concentrations. To extend this method assume that there exists a tensor such that

$$\bar{\varepsilon}^{(2)} \approx M\bar{\varepsilon}^{(1)}. \tag{1.88}$$

Using Eqs. (1.87) and (1.88) we get

$$A_2 = M\left[c_1 I + c_2 M\right]^{-1}. \tag{1.89}$$

If it is further assumed that

$$M = T \tag{1.90}$$

then

$$C^* = C^{(1)} + c_2(C^{(2)} - C^{(1)})T(c_1 I + c_2 T)^{-1}, \tag{1.91}$$

and similarly for the effective compliance tensor. Benveniste showed that these results are consistent in the sense that

$$S^* = (C^*)^{-1}. \tag{1.92}$$

Finally,

$$\frac{\bar{\varepsilon}_{kk}^{(2)}}{\varepsilon_{kk}^{(1)}} = \frac{3K_1 + 4\mu_1}{3K_2 + 4\mu_1} \tag{1.93}$$

and the effective bulk modulus is

$$K^* = K_1 + c_2(K_2 - K_1)\frac{K_1}{(1 - c_2)(K_2 - K_1)\alpha_1 + K_1}, \tag{1.94}$$

and

$$\alpha_1 = \frac{3K_1}{(3K_1 + 4\mu_1)}, \tag{1.95}$$

See Aboudi (1991) for additional details.

1.3.10. Others. Other methods that are mentioned with some regularity in the literature are the Composites Sphere Model, (Hashin, 1962), Lamination Theory, (see for example, Herakovich, 1998) and Periodic Unit Cell Models. An example of the last will be presented in the third lecture.

2. Stochastic micromechanics

While statistical averaging lies at the heart of classical micromechanics, the predictions of classical micromechanics are fundamentally deterministic. It makes sense, therefore, to reformulate and explore these problems in a stochastic framework. This has been done to a certain extent in texts on Stochastic Mechanics and the Mechanics of Heterogeneous Materials. This includes the development of stochastic differential equations, homogenization theory and, the use of stereology and stochastic geometry.

Classical micromechanics makes some fairly strong, limiting assumptions about the shapes of an included phase, the specific interactions between, for example between particles and between particles and matrix, and the spatial arrangement of the included phase within a matrix. This lack of a

detailed description limits classic micromechanical analysis, including any potential predictions based on the effects of local response. So, from the perspective of Classical Micromechanics, the next level of modelling needs more detailed descriptions of the random patterns of the spatial arrangement of the microstructure. Stereology and stochastic geometry offer powerful tools such descriptions.

Since others in this lecture series, and referenced in this series, have a great deal of expertise in the derivation, understanding and application of stochastic modeling of microstructure, (see for example Sobczyk and Kirkner, 2001, and Torquato, 2002), this work will not attempt a presentation. Instead what will be presented is first, some of the parallel terms of micromechanics and stochastic micromechanics and second, a set of examples which illustrate the directions applications of stochastic modelling have taken.

2.1. Concepts

The primary and fundamental assumption made in the stochastic literature is that one is dealing with ergodic media. A sample record (microstructure) of a random physical process can be thought of as a physical realization of the random process.

An *Ergodic Hypothesis* is then assumed; if the result of averaging over all realizations of the process is equivalent to averaging over one realization, as the volume goes to infinity, then the medium can be considered ergodic. This is a mathematically rigorous statement of what is an underlying concept in classical micromechanics; captured there in the notion of an RVE.

Additionally, the literature characterizes media as *spatially stationary* or strictly *statistically homogeneous*. This implies that the properties do not depend on the absolute position of specific microstructural elements; in other words that the joint probability density fields are invariant under translation. From the point of view of classical micromechanics, statistical homogeneity is probably mostly aligned with the notion that the material has effective properties; i.e., that it can be homogenized. Other concepts that have parallel forms in stochastic mechanics are:

The *probabilistic mean* is defined as

$$m_x(r) = \langle X(r,\gamma)\rangle = \int_{\Gamma} X_r(\gamma) dP_r(\gamma), \tag{2.1}$$

$$m_x(r) = \int x_r f_r(x) dx \tag{2.2}$$

where $f_r(x)$ is the density function for the realization, $x_\gamma(r)$. $\gamma \in \Gamma$, which

is the space of elementary events on which the probability P is defined. The symbol $\langle\cdot\rangle$ denotes averaging.

Multiple realizations may not be feasible for most applications. However, for an ergodic medium, over a large volume, the probabilistic mean is equivalent to a volume average.

$$\frac{1}{m(S_1)\rho^n}\int_{S_\rho} X(r)dr \to E[X_r], \quad \text{as} \quad \rho \to \infty. \tag{2.3}$$

Here S_ρ is the sphere of radius ρ, and $m(S_1)$ is the volume of the unit sphere.

Averages of local field variables are uniform for ergodic fields so stress and strain can be written as the sum of an average term, $\langle\cdot\rangle$, and a fluctuating term, $(\cdot)'$.

$$\varepsilon = \langle\varepsilon\rangle + \varepsilon', \qquad \sigma = \langle\sigma\rangle + \sigma' \tag{2.4}$$

where the averages of the fluctuating terms are zero. This can be used to show that with ergodicity, the fluctuation terms are zero on the boundary.

The idea of "effective properties" is formulated using the theory of homogenization. This theory takes into consideration, in the case of the simplest microstructural form, three length scales. First are the macroscopic L and the microscopic, l characterizes the extent of the bulk material and l characterizes the scale of the heterogeneity. It is then assumed that any external fields vary on a characteristic length scale λ. Where

$$l \ll \lambda \leqslant L. \tag{2.5}$$

A small parameter can then be defined associated with the small scale changes in the microstructure or associated property, $\epsilon = l/L$. The field quantities (e.g. stress field) can then be thought of as depending on the global or slow variable, x, (spatial position), and a local or fast variable $y = x/\epsilon$. The slowly varying parts are due to the external fields, the fast parts vary due to the microstructural variations, and characterize the associated local property. The stiffness tensor, for a given realization ω, is defined as a rapidly fluctuating function of position,

$$C^\epsilon(x) = C(y;\omega), \quad y = x/\epsilon, \tag{2.6}$$

for each realization the equilibrium equation is satisfied, thus

$$\frac{\partial}{\partial x_j}\left[C^\epsilon_{ijkl}(x)\varepsilon^\epsilon_{kl}(x)\right] = 0 \tag{2.7}$$

in the absence of body forces. When the medium is ergodic and statistically homogeneous then C_e is an effective stiffness tensor, such that if the

solution of

$$\varepsilon_{kl}^{(0)}(x) = \frac{1}{2}\left(\frac{\partial u_j^{(0)}}{\partial x_i} + \frac{\partial u_i^{(0)}}{\partial x_j}\right) \tag{2.8}$$

satisfies the deterministic equation

$$\left[(C_e)_{ijkl}\frac{\partial}{\partial x_j}\varepsilon_{kl}^{(0)}(x)\right] = 0, \tag{2.9}$$

then

$$\int_V \left\langle |u^\epsilon(x) - u^{(0)}(x)|^2 \right\rangle dx \to 0, \quad \text{as} \quad \epsilon \to 0. \tag{2.10}$$

In other words, an ergodic medium behaves like a homogeneous deterministic medium with effective properties when ϵ becomes small. This can be demonstrated by using a two scale asymptotic expansion of the displacement and substituting into the differential equation. The net result is that the effective stiffness tensor is defined by the relationship

$$\langle \sigma(x) \rangle = C_e \langle \varepsilon(x) \rangle \tag{2.11}$$

where

$$(C_e)_{ijkl} = \langle C_{ijkl} \rangle + \left\langle C_{ijmn}\frac{1}{2}\left(\frac{\partial \chi_{kmn}}{\partial y_l} + \frac{\partial \chi_{lmn}}{\partial y_k}\right)\right\rangle \tag{2.12}$$

and χ_{kmn} satisfies

$$-\frac{\partial}{\partial y_l}\left[C_{ijkl}(y;\omega)\frac{1}{2}\left(\frac{\partial \chi_{kmn}}{\partial y_l} + \frac{\partial \chi_{lmn}}{\partial y_k}\right)\right] = \frac{\partial}{\partial y_l}C_{ijmn}(y;\omega). \tag{2.13}$$

(Following Torquato, 2002).

2.2. Bounds

The idea of bounding the effective properties has also been studied using stochastic techniques. Hashin–Shrikman (1963) bounds, which were developed using variational principles, can also be found in the stochastic mechanics literature. As mentioned before, the power of these bounds lies in the minimal input information required; for Hashin–Shrikman bounds, the elastic properties of the individual phases and the relative volume fractions are required.

Beran and Molyneux (1966) developed bounds on the effective properties defined by

$$K^* \leqslant \langle K(r,\gamma)\rangle - \frac{\left\langle K'^2(r,\gamma)\right\rangle}{\langle \lambda(r,\gamma)\rangle + 2\langle \mu(r,\gamma)\rangle + \dfrac{\langle \lambda'(r,\gamma)K'^2\rangle}{\langle K'^2\rangle} + \dfrac{2I}{\langle K'^2\rangle}} \tag{2.14}$$

where

$$I = \frac{1}{16\pi^2} \int_r \int_s \frac{1}{|r||s|} \frac{\partial^2}{\partial r_i \partial r_j} \frac{\partial^2}{\partial s_i \partial s_j} \left\langle \mu'(0,\gamma) K'(r,\gamma) K'(s,\gamma) \right\rangle dr ds \quad (2.15)$$

and

$$r_i = x_i - x_i', \quad r = (x_1, x_2, x_3), \quad s = (x_1', x_2', x_3'). \quad (2.16)$$

The integral in equation (2.15) represents the third order correlation function (three point correlation function). These bounds, therefore, provide a more accurate measure based on the spatial pattern associated with the microstructure.

2.3. Simulating the microstructure

In the engineering community, characterizing microstructures has, by and large, followed one of two paths. First, many materials scientists, including soil mechanicians and other investigators in granular or porous media, have based statistical characterizations on real microstructural images. Stereology has generally been used to refer to the inference of three dimensional characteristics from two dimensional images. With the advent of high speed, large memory computers it is now fairly simple to use two dimensional sectioning to characterize stochastic properties that can be used to build a three dimensional digital reconstruction. Similarly, but more expensively, computer tomography may be used to non-destructively record a three-dimensional digital image. From these images statistical metrics can be derived, (e.g. mean values, correlation functions, n-point probability functions). Scores of students have, in elementary material science classes, been handed a micrograph and asked to count dark and light pixels, in grid regions, to toss rods (randomly place lines) on the image and count the number of times both ends fall in the same phase. Fortunately, computers have also facilitated this process and commercial software programs exist that can perform many of these computations accurately and efficiently. Computational mechanics then offers many ways to incorporate these reconstructed microstructures into, for example, finite element codes.

The second direction has been to use known probabilistic descriptors from ideal materials to illustrate and characterize real microstructures. In this case, field statistical structure is assumed and a simulated material is generated. These metrics can then be used to derive bounds of the effective properties.

2.3.1. Statistical reconstruction. Reconstructing digital samples of materials using given stochastic properties has a number of advantages. This

approach minimizes the need for three dimensional digital files of multiple samples, which may be difficult to obtain, it can allow the generation of 3-D samples from 2-D measurements, and it can help to establish the choice of stochastic functions that will most accurately characterize specific material properties.

A great deal of the well-referenced work in the literature on statistical reconstruction has been done by researchers interested in porous materials. One fundamental reference is Quiblier (1983), which presents a very clear outline of how information from sectioning can be derived and used in simulation. He modeled a matrix material with voids.

The aim of this work was to simulate, with a random process, a porous medium that was geometrically realistic and well-defined, in other words, it is clear to which phase each spatial location belongs. Using the gray scale levels of the digital image, two statistical measurements were established. First, a discrete probability density function (PDF) was generated by classifying the numeric values associated with the digital image (gray scale values) into a small number of classes and calculating the relative frequency for each class. Second, an autocorrelation function (ACF) was calculated, using

$$f(H) = \frac{E\{[z(P+H) - m] \cdot [z(P) - m]\}}{E\left\{[z(P) - m]^2\right\}} \tag{2.17}$$

where m is the mean value, $z(P)$ is the gray scale value at the point P, and $(P+H)$ is position incrementally off of the point P. The rough translation is that this function contains information about the probability that the point $(P+H)$ is in a matrix region, if the point P is in a matrix region.

These two functions are extremely useful because they are the same for 2-D and 3-D if the material is isotropic. This does not mean that the process was limited to isotropic samples, because anisotropy can be developed by examining several mutually perpendicular sections. Quiblier does make the assumption that the microstructure can be characterized by a stationary field.

The simulation is performed in the following way. First random numbers $x(i,j,k)$ are generated at each point on a grid (i,j,k) in, for example, a cube domain. These numbers are uncorrelated but were created as a Gaussian population with a mean value of 0 and a variance of 1. Next a neighboring region was considered which included the points $(i+r, j+s, k+t)$. The size of this neighborhood corresponds to a small distance outside of the distance at which the ACF is negligible. The values of $x(i+r, j+s, k+t)$ are linearly

combined to form a new number $y(i,j,k)$ defined by

$$y(i,j,k) = \sum_{r,s,t} a(r,s,t) \cdot x(i+r, j+s, k+t). \tag{2.18}$$

This set of y values can be demonstrated to be Gaussian, because the set on which it was built, x was Gaussian. It is different from the set x in that the y values are now correlated. It can also be shown that the coefficients $a(r,s,t)$ can be chosen to match the ACF of y to the ACF of the original sample. Quiblier refers to this as "linear filtering". A second transformation is necessary to map the set y from a Gaussian PDF to one that matches the PDF of the original sample. He does this by using "nonlinear filtering". Given a histogram (Fig. 1) of the relative frequencies (a discrete PDF), a cumulative PDF can be constructed. The nonlinear filtering results in a system of nonlinear equations and is illustrated in Fig. 2.

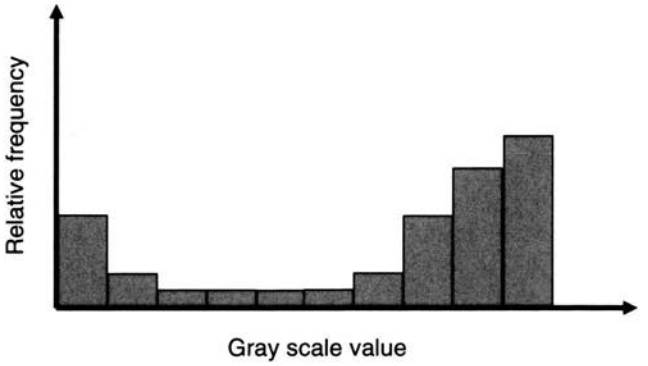

FIGURE 1. Histogram of gray scale values from digital image of section.

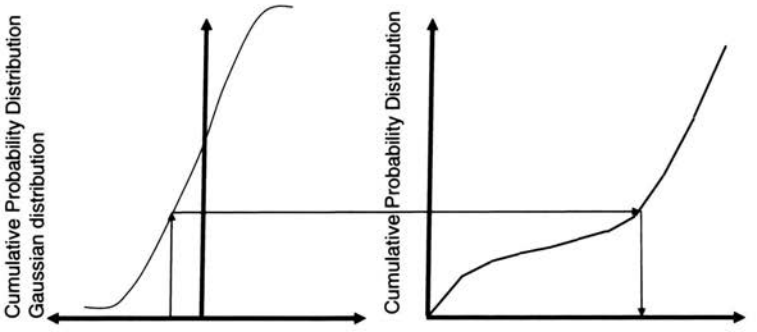

FIGURE 2. Schematic of mapping from Gaussian to Data based PDF.

The set of data y, thus transformed, is then the simulated data set. Quiblier (1983) provides appendices that detail the steps of the linear and nonlinear filtering. The general idea of this method, applying linear and non-linear filtering techniques to an originally normalized Gaussian field, was extended by Adler et al. (1990) who also refined the model to employ periodic boundary conditions.

Manwart, Torquato and Hilfer (2000) used an annealing algorithm (Rintoul and Torquato, 1997) to reconstruct Brea and Fontainebleau sandstone also using metrics measured from real samples of the material. Their goal was to evaluate the choice of stochastic functions used in the reconstruction. A comparison of several characteristics of the real and simulated samples is included in the article. They assumed their materials were homogeneous, stationary, ergodic, stochastic media. Their choice of stochastic functions was first, a two point probability function defined as

$$S_2(\vec{x}_1, \vec{x}_2) = \langle \chi(\vec{x}_1)\chi(\vec{x}_2) \rangle \tag{2.19}$$

where the angular brackets denote a volume average, and the function $\chi(\vec{x})$ is the characteristic function

$$\chi(\vec{x}) = \begin{cases} 0 & \text{for } \vec{x} \in \text{matrix}, \\ 1 & \text{for } \vec{x} \in \text{voids}. \end{cases} \tag{2.20}$$

This function forces the specific surface areas (interface between phases) of the reconstructions to match those of the reference sample. Their second stochastic function was a lineal-path function, $L(r)$. This function is defined as the probability of finding a line segment of length r entirely in one phase, when it is randomly placed on the random medium. It can be calculated by counting the number of voxels, (3-D pixel) that lie between a pore voxel and the nearest matrix voxel in a coordinate direction. The function is given by

$$L(r) = \frac{l(r)}{[(M_1 - r)(M_2 M_3 + M_1(M_2 - r)M_3 + M_1 M_2(M_3 - r)} \tag{2.21}$$

where $l(r)$ is the number of line segments with length r, and M_1, M_2, and M_3 are the sample dimensions in pixels. This function incorporates information about the connectivity of the sample, important for porous materials.

They also constructed a pore distribution function, $P(\delta)$ which measured the probability that a randomly chosen point in a pore lies a specific distance δ from a matrix pore interface. This was done by making random measurements at discrete points and constructing a histogram. In each of the above periodic boundary conditions were assumed.

The reconstruction was performed iteratively. It started with a random configuration, and at each iteration step, two voxels from different phases were interchanged. There is a criteria by which this new configuration is either accepted or rejected based on the minimization of a target energy function. If changes are rejected consecutively for more than a pre-defined number of times the reconstruction is complete.

Their conclusions were that in general the morphology of the reconstructed samples was in good agreement with the real samples, but that the match in connectivity compared between the two types of samples was not good.

There is a third class of reconstruction techniques, those that specifically capture the underlying physics of the material formation. Models of this type can be found in some of the literature using cellular automata which incorporate probabilistic decision making rules.

2.3.2. Model composite materials. Other studies have taken the approach of describing more idealized microstructures that provide realistic representation of many classes of microstructure. From these models statistical information is calculated and can be used to bound effective properties. Examples include the overlapping solid sphere model, spherical pores, and level-cut Gaussian random fields. Descriptions of models of this type can be found in for example, Roberts, and Knackstedt (1996), Roberts and Garboczi, (2002), Roberts and Teubner (1995), and Torquato (1991).

2.4. Structure property connection

In all of the approaches described above useful microstructural models have been generated, reconstructed or simulated. The main issue in micromechanics however is the structure-property relationship. Classical micromechanics provides this, but the influence of specific microstructures is largely omitted. Homogenization techniques also provide a rigorous method of developing effective properties, but again, have minimal input of detailed microstructural description.

Statistical reconstruction and model composite materials offer more detailed microstructural descriptions, but there is no inherent link from these more complete descriptions to the behavior of the material. What has traditionally been done is either to calculate the third order correlation function needed for the Beran-Molyneux bounds or other bounds (See Roberts and Teubner 1995, Torquato 2002) , or used the generated microstructures as the mesh in finite element models of the material. These models include those designed to handle 3-D mesh structures or arbitrary voxels (Garboczi and

Day 1995, Garboczi 1998). Povirk (1995) developed a method for determining periodic microstructures that are statistically similar to more complex, random, two-phase microstructures and constructed finite element models that used a representative unit cell.

In the next section a slightly different approach to including both the influence of a specific microstructure as well as establishing a structure property relationship is presented.

3. Current research: Moving Window micromechanics

The strengths of classical micromechanics lie in its rigor, straight-forward implementation and input. Its weaknesses are in the limited microstructural detail that the models capture, and a general inability to obtain local information based on the spatial arrangements. Stochastic modeling of microstructure offers the power of a detailed and non-deterministic model of the microstructure, which is useful for simulations and computational modeling of material structure. Its main limitation is that there is no inherent connection from the statistics of the microstructure to the material properties.

We wanted something that could capture the variability of the local response due to the microstructure, which classical micromechanics did not, but which also did not require dealing with the complexity of microstructural detail, e.g., particle shapes, sizes, orientations and spatial arrangement.

Our solution was to use classical micromechanics to generate local effective properties based on the microstructure, and then analyze the *statistics of these property fields*, rather than of the statistics of the spatial geometry and architecture of the microstructure (Baxter and Graham, 2000). The strength of this approach is that the material property fields are easy to import into a, or to characterize for, an FE model with regular grids, they can be consistently developed from real microstructural images, and their characterization can provide the basis for simulations of additional material samples.

First generation material property fields could be created by assigning the material properties of each phase to the pixel locations associated with that phase. While these fields are the most accurate representation based on the digitized image, they are extremely noisy; in the limiting case of a two-phase composite, a two-point field is generated. The statistics on such fields are difficult to develop, there is no consistent methodology recommended in the literature and the use of these fields in a finite element context may lead to unrealistic results due to stress concentrations that occur at abrupt material interfaces. These issues motivated the use of a moving-window technique in order to provide local characterization of the effects of the microstructure on

the mechanical properties. Moving-window techniques have recently emerged as a useful technique for characterizing random composite microstructure, based purely on a digitized microstructural image (e.g., Graham & Baxter 1998, Lu & Torquato 1990, Ostoja-Starzewski 1994, Ostoja-Starzewski & Wang 1999, Tang & Gilbert 1989). These methods offer the major advantage that no assumptions need to be made as to the shapes, sizes or placement of inclusions. The only constraints in such moving-window analyses are that multiple phases of the composite are visually differentiable and that their individual constitutive behavior is known.

3.1. Method overview

Using a material micrograph in which the phases are visually distinguishable, small subsets, "windows" of the image are analyzed using a classical micromechanical analysis. The resulting effective material properties of the "window" are then assigned to the center coordinates of the window. Windows overlap, the idea is to capture the influence of neighboring microstructure, and the fields are created by rastering the windows over the micrograph. Periodic boundary conditions are not assumed and so the net result is a cropped field of properties, relative to the original sample.

The numerically generated sample shown in Fig. 3, represents a transverse section of a continuous fiber reinforced composite. The white regions are fibers; the black region is matrix material. By assigning the image the properties of a silicon-carbide fiber reinforced titanium matrix, property fields were generated to illustrate the moving window methodology. These fields are shown in Fig. 4. A window size of 5% × 5% of the total 200 by 200 pixels^2 was used.

It is clear from these plots that the axial modulus and the fiber volume fraction are very well correlated. The spatial variations in the transverse elastic moduli are also correlated to fiber volume fraction, but unlike the axial elastic modulus is not as visible a function of the volume fraction. A rule of mixtures approach would therefore be inappropriate for consideration of the transverse elastic moduli.

The fields can be statistically characterized by, for example, mean value, auto- and cross-correlation functions. In the graphs below, a homogeneous random field is assumed:

$$E_{yy}(z,y) = E^0_{yy}\big(1 + f_y(z,y)\big). \tag{3.1}$$

Here E^0_{yy} is the mean elastic modulus and $f_y(z,y)$ is a zero-mean stochastic field that describes the fluctuation of the elastic modulus about its mean value.

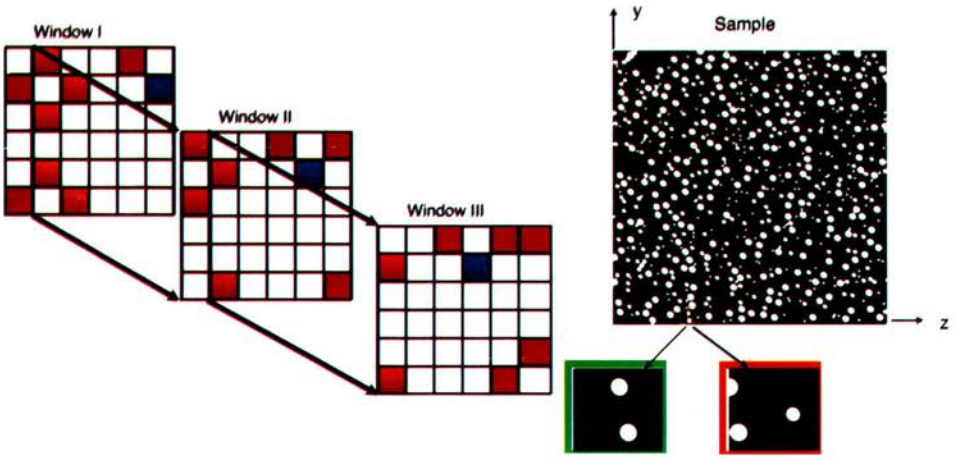

FIGURE 3. Diagram of moving window methodology. Windows overlap, rastered over entire field.

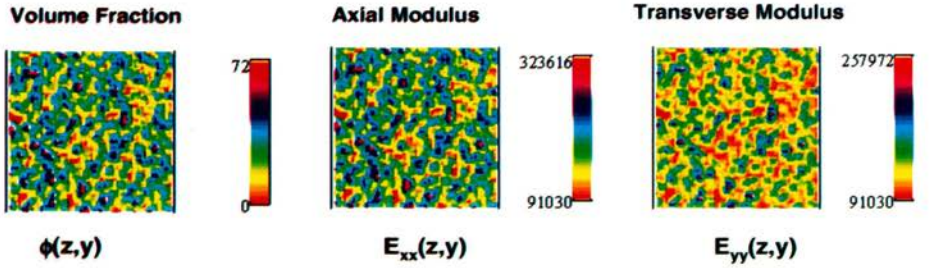

FIGURE 4. Sample fields from MW analysis. Volume fraction and elastic moduli. (The plane is y-z and x is the axial direction).

Figure 5 shows the auto-correlation function

$$\rho_{f_x f_x}(\Delta y, \Delta z) = E\left[f_y(y_1, z_1) \cdot f_y(y_1 + \Delta y, z_1 + \Delta z)\right] \tag{3.2}$$

corresponding to the axial elastic modulus and to the transverse elastic modulus respectively. $E[\cdot]$ is the expected value. These plots are based on a moving window size $5\% \times 5\%$ of the total sample length. For this relatively small window size the correlation functions die down to zero very rapidly, supporting the assertion that these fields are ergodic in the mean.

In an area with a high value for the axial elastic modulus, E_{xx}, it is reasonable to expect that the transverse elastic moduli, E_{yy}, E_{zz} will be higher as well. Based on the elastic modulus fields generated, the cross-correlation functions describing correlation between the axial elastic modulus and the

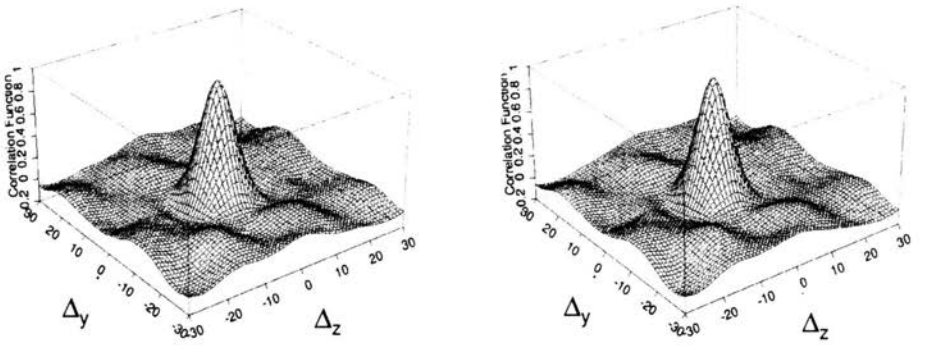

FIGURE 5. Auto correlation functions for axial (x) modulus and (R) and transverse (z) moduli.

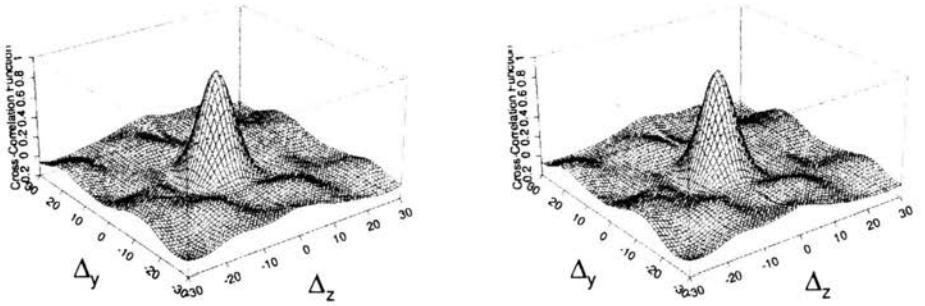

FIGURE 6. Cross correlation function (L) between axial and transverse (y) modulus, (R) between axial and transverse modulus (z).

transverse elastic moduli were calculated and are plotted in Fig. 6. The two properties are also very well correlated.

3.2. The effect of window size

The dominant parameter in the moving-window micromechanics technique is the size of the window. Windows that are too small represent noisy fields, and may be computationally less tractable. Windows that are too large produce less variation in the fields and can, in the limit, result in effective properties that mask the local effects of the heterogeneous microstructure.

A comparison of the fields associated with the microstructure in Fig. 3, produced using three different window sizes is shown in Fig. 7. As the window size increases, the field becomes smoother and the range of values for E_{yy} decreases. There is a corresponding decrease in the calculated mean value and variance of the elastic moduli as well.

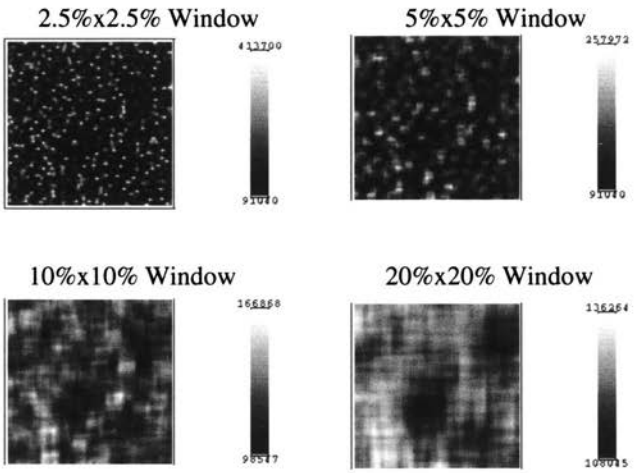

FIGURE 7. Plot of Transverse Elastic Modulus E_{yy}, based on: 2.5% × 2.5%, 5% × 5%, 10% × 10%, and 20% × 20% window size.

3.3. Micromechanics model: Method of Cells

The basic work was done using the micromechanics model known as the Generalized Method of Cells (GMC, Paley and Aboudi, 1992). This model is an extension of the original method of cells (MOC, Aboudi, 1989), both are periodic unit cell models. In what follows, the methodology behind the original MOC is presented; because it is simpler to describe, but exactly analogous to GMC.

In the MOC, four subcells are used as a repeating cell to describe a doubly periodic material (continuous fiber composite). Each subcell takes on the properties of a single phase with known constitutive properties. In Fig. 8 below, the gray subcell is the fiber, the white subcells are the matrix. By

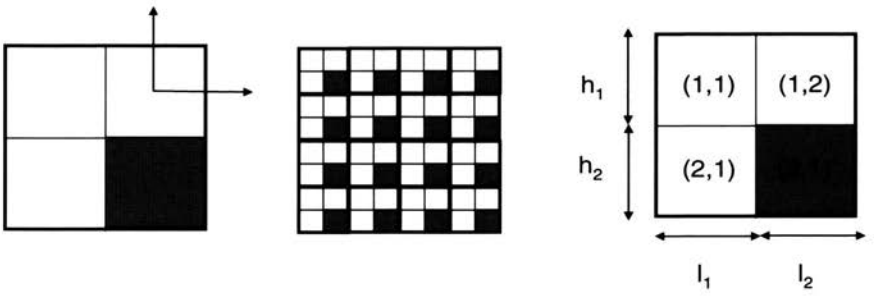

FIGURE 8. (Left:) Unit cell of MOC. (Centre:) unit cell repeated to generate square array of fibers. (Right:) dimensions and numbering of unit cells.

stamping this pattern out in two orthogonal directions a square array of a transverse view of the fibers appears. Subcell dimensions can be set, h_i, l_i, and each subcell is matrix numbered (β, γ). A local coordinate system is associated with each subcell.

Beginning at the micro level, the displacement, $w_i^{(\beta,\gamma)}$, of the center of each subcell is described by a first order expansion

$$u_i^{(\beta,\gamma)} = w_i^{(\beta,\gamma)} + \bar{x}_2^{(\beta)}\phi_i^{(\beta,\gamma)} + \bar{x}_3^{(\gamma)}\psi_i^{(\beta,\gamma)}, \quad i = 1,2,3, \tag{3.3}$$

where $\phi_i^{(\beta,\gamma)}$ and $\psi_i^{(\beta,\gamma)}$, are microvariables which characterize the dependence of this center point displacement on the local coordinates, $\bar{x}_2^{(\beta)}$ and $\bar{x}_3^{(\gamma)}$. Using the local strain-displacement equation for each subcell, the microvariables can be shown to be related to the subcell strains as

$$\varepsilon_{11}^{(\beta,\gamma)} = \frac{\partial w_1^{(\beta,\gamma)}}{\partial x_1}, \qquad \varepsilon_{22}^{(\beta,\gamma)} = \phi_2^{(\beta,\gamma)}, \qquad \varepsilon_{33}^{(\beta,\gamma)} = \psi_3^{(\beta,\gamma)}, \tag{3.4}$$

$$2\varepsilon_{12}^{(\beta,\gamma)} = \phi_1^{(\beta,\gamma)} + \frac{\partial w_2^{(\beta,\gamma)}}{\partial x_1}, \tag{3.5}$$

$$2\varepsilon_{13}^{(\beta,\gamma)} = \psi_1^{(\beta,\gamma)} + \frac{\partial w_3^{(\beta,\gamma)}}{\partial x_1}, \tag{3.6}$$

$$2\varepsilon_{23}^{(\beta,\gamma)} = \phi_3^{(\beta,\gamma)} + \psi_2^{(\beta,\gamma)}. \tag{3.7}$$

Assuming an homogenization condition (see Aboudi 1982, 1991 for more details),

$$w_i^{(1,1)} = w_i^{(1,2)} = w_i^{(2,1)} = w_i^{(2,2)} = w_i, \tag{3.8}$$

imposing continuity of displacements

$$\begin{aligned} h_1\varphi_i^{(1,\gamma)} + h_2\varphi_i^{(2,\gamma)} &= (h_1 + h_2)\frac{\partial w_i}{\partial x_2}, \\ l_1\psi_i^{(\beta,1)} + l_2\psi_i^{(\beta,2)} &= (l_1 + l_2)\frac{\partial w_i}{\partial x_3}, \\ \bar{\varepsilon}_{ij} &= \frac{1}{2}\left(\frac{\partial w_i}{\partial x_j} + \frac{\partial w_j}{\partial x_i}\right), \end{aligned} \tag{3.9}$$

continuity of tractions across subcell boundaries (periodic boundary conditions will wrap around the unit cell boundaries)

$$\bar{\sigma}_{2i}^{(1,\gamma)} = \bar{\sigma}_{2i}^{(2,\gamma)}, \qquad \bar{\sigma}_{3i}^{(\beta,1)} = \bar{\sigma}_{3i}^{(\beta,1)}, \tag{3.10}$$

and using the known subcell constitutive laws, the local stresses can be written in terms of microvariables as

$$\begin{aligned}
\bar{\sigma}_{11}^{(\beta,\gamma)} &= C_{11}^{(\beta,\gamma)}\bar{\varepsilon}_{11} + C_{12}^{(\beta,\gamma)}\left(\varphi_2^{(\beta,\gamma)} + \psi_3^{(\beta,\gamma)}\right), \\
\bar{\sigma}_{22}^{(\beta,\gamma)} &= C_{12}^{(\beta,\gamma)}\bar{\varepsilon}_{11} + C_{22}^{(\beta,\gamma)}\varphi_2^{(\beta,\gamma)} + C_{23}^{(\beta,\gamma)}\psi_3^{(\beta,\gamma)}, \\
\bar{\sigma}_{33}^{(\beta,\gamma)} &= C_{12}^{(\beta,\gamma)}\bar{\varepsilon}_{11} + C_{23}^{(\beta,\gamma)}\varphi_2^{(\beta,\gamma)} + C_{22}^{(\beta,\gamma)}\psi_3^{(\beta,\gamma)}, \\
\bar{\sigma}_{12}^{(\beta,\gamma)} &= C_{44}^{(\beta,\gamma)}\left(\frac{\partial w_2}{\partial x_1} + \varphi_1^{(\beta,\gamma)}\right), \\
\bar{\sigma}_{13}^{(\beta,\gamma)} &= C_{44}^{(\beta,\gamma)}\left(\frac{\partial w_3}{\partial x_1} + \psi_1^{(\beta,\gamma)}\right) \\
\bar{\sigma}_{23}^{(\beta,\gamma)} &= C_{66}^{(\beta,\gamma)}\left(\psi_2^{(\beta,\gamma)} + \varphi_3^{(\beta,\gamma)}\right).
\end{aligned} \tag{3.11}$$

With a lot of ugly algebra and arithmetic, and the equations for average stress and strain it is possible to write the effective properties tensor **b**, such that

$$\begin{aligned}
\bar{\sigma}_{11} &= b_{11}\bar{\varepsilon}_{11} + b_{12}\bar{\varepsilon}_{22} + b_{13}\bar{\varepsilon}_{33}, \\
\bar{\sigma}_{22} &= b_{12}\bar{\varepsilon}_{11} + b_{22}\bar{\varepsilon}_{22} + b_{23}\bar{\varepsilon}_{23}, \\
\bar{\sigma}_{33} &= b_{13}\bar{\varepsilon}_{11} + b_{32}\bar{\varepsilon}_{22} + b_{33}\bar{\varepsilon}_{33},
\end{aligned} \tag{3.12}$$

The elements of **b**, contain terms that describe the composite geometry and include the influence of the constitutive properties of the subcells and can be written out in closed form. (See Aboudi, 1991.)

The Generalized Method of Cells incorporates an arbitrary number of subcells, which allows multi-phase (> 2) materials to be modelled, and more complex geometries to be described. Closed form expressions are not available for GMC, the solution involves a large system of equations, but the idea is the same; the mechanics is established at the microscale and built up to the macroscale.

3.4. Embedding the micromechanics

It should be emphasized that the Moving Window Technique does not satisfy the assumptions of classical micromechanics and is not mathematically rigorous. In particular, the windows are not RVEs, boundary conditions for each window cannot be absolutely established and the method uses infinite domain micromechanics for a finite domain problem. The method can only

be considered an averaging scheme where local contributions are *weighted* using micromechanics.

One major issue that can be examined is the choice of micromechanics model used in the moving window. In Graham, Siragy and Baxter (2003), three models were considered and their relative differences compared. The three micromechanical models were GMC, Mori–Tanaka, and a brute force finite element model used with windowing.

A clustered microstructure (Fig. 10) was considered with fibers of approximately 6 pixels in diameter with a 25% fiber volume fraction. For the numerical work the properties of a SiC/TI composite were used. In this work the transverse plane is x_1-x_2.

Using engineering notation the following general constitutive law was assumed

$$\begin{Bmatrix} \sigma_{11}(x_1,x_2) \\ \sigma_{22}(x_1,x_2) \\ \tau_{12}(x_1,x_2) \end{Bmatrix} = \begin{bmatrix} C_{11}(x_1,x_2) & C_{12}(x_1,x_2) & C_{13}(x_1,x_2) \\ C_{21}(x_1,x_2) & C_{22}(x_1,x_2) & C_{23}(x_1,x_2) \\ C_{31}(x_1,x_2) & C_{32}(x_1,x_2) & C_{33}(x_1,x_2) \end{bmatrix} \begin{Bmatrix} \varepsilon_{11}(x_1,x_2) \\ \varepsilon_{22}(x_1,x_2) \\ \gamma_{12}(x_1,x_2) \end{Bmatrix} \tag{3.13}$$

where the subscript 3 refers to a component of shear.

Using Mori–Tanaka (MT), homogeneous boundary conditions and circular fiber cross sections are assumed. The limitations of this model are that there is no coupling of shear and normal stresses and strains, and the local anisotropy is limited to transverse isotropy.

The resulting constitutive law looks like

$$C^{\text{Mori–Tanaka}}(x_1,x_2) = \frac{1}{\Delta_1(x_1,x_2)} \begin{bmatrix} E - E_{33}\nu_{13}^2 & E\nu_{12} + E_{33}\nu_{13}^2 & 0 \\ E\nu_{12} + E_{33}\nu_{13}^2 & E - E_{33}\nu_{13}^2 & 0 \\ 0 & 0 & G_{12} \end{bmatrix} \tag{3.14}$$

where

$$E = E_{11}(x_1,x_2) = E_{22}(x_1,x_2) \tag{3.15}$$

and

$$\Delta_1(x_1,x_2) = 1 - \nu_{12}^2 - \frac{E_{33}}{E}\left(2\nu_{13}^2 + 2\nu_{12}\nu_{13}^2\right). \tag{3.16}$$

E, G, and ν are the engineering constants, the Young's modulus, shear modulus and Poisson's ratio, respectively.

When using GMC, the assumptions are of periodic boundary conditions. The fiber shapes are captured in more detail than MT via the digital image. Like MT, GMC is limited in that no coupling of shear and normal stresses and strains exists. GMC is less limiting than MT in that it restricts the local anisotropy to orthotropy.

The resulting constitutive law is

$$C^{\mathrm{GMC}}(x_1,x_2)=\begin{bmatrix} \dfrac{E_{22}-E_{33}\nu_{13}^2}{E_{22}^2E_{33}\Delta_2} & \dfrac{E_{11}\nu_{12}+E_{33}\nu_{13}^2}{E_{11}E_{22}E_{33}\Delta_2} & 0 \\ \dfrac{E_{11}\nu_{12}+E_{33}\nu_{13}^2}{E_{11}E_{22}E_{33}\Delta_2} & \dfrac{E_{11}-E_{33}\nu_{13}^2}{E_{11}^2E_{33}\Delta_2} & 0 \\ 0 & 0 & G_{12} \end{bmatrix} \tag{3.17}$$

where

$$\Delta_2(x_1,x_2)=\frac{E_{11}E_{22}-E_{22}^2\nu_{12}^2-E_{11}E_{33}\nu_{13}^2-E_{22}E_{33}\nu_{13}^2-2E_{22}E_{33}\nu_{12}\nu_{13}^2}{E_{11}^2E_{22}^2E_{33}}, \tag{3.18}$$

In order to create a comparable model using a finite element (FE) model, a plane strain analysis was performed on the entire microstructure. Three loading conditions were used to generate the full stiffness matrix, uniaxial tension in the two in-plane directions and an in-plane shear. Each of the models used a combination of displacement and traction boundary conditions. A moving window analysis, with the same window size as the other models, was then used to average the local properties.

The constitutive law for this model is

$$\begin{aligned} C^{\mathrm{FE}}(x_1,x_2)=&\left[\sigma_{\mathrm{avg}}^{\mathrm{AX1}}(x_1,x_2)\quad \sigma_{\mathrm{avg}}^{\mathrm{AX2}}(x_1,x_2)\quad \sigma_{\mathrm{avg}}^{\mathrm{SHR}}(x_1,x_2)\right]\\ &\cdot\left[\varepsilon_{\mathrm{avg}}^{\mathrm{AX1}}(x_1,x_2)\quad \varepsilon_{\mathrm{avg}}^{\mathrm{AX2}}(x_1,x_2)\quad \varepsilon_{\mathrm{avg}}^{\mathrm{SHR}}(x_1,x_2)\right]^{-1} \end{aligned} \tag{3.19}$$

where

$$\begin{aligned} &\sigma_{\mathrm{avg}}^{\mathrm{AX1}}(x_1,x_2), \qquad \varepsilon_{\mathrm{avg}}^{\mathrm{AX1}}(x_1,x_2),\\ &\sigma_{\mathrm{avg}}^{\mathrm{AX2}}(x_1,x_2), \qquad \varepsilon_{\mathrm{avg}}^{\mathrm{AX2}}(x_1,x_2),\\ &\sigma_{\mathrm{avg}}^{\mathrm{SHR}}(x_1,x_2), \qquad \varepsilon_{\mathrm{avg}}^{\mathrm{SHR}}(x_1,x_2) \end{aligned} \tag{3.20}$$

correspond to the averages from the three loading states, axial tension in 1-direction, the 2-direction and shear loading.

The resulting fields for each of the three models are virtually indistinguishable, however some comparisons are possible.

3.4.1. Comparison problems

Field errors

To illustrate the effect of the window size, the error in moving-window Mori–Tanaka and in moving-window GMC, relative to the brute-force FEA,

(a)

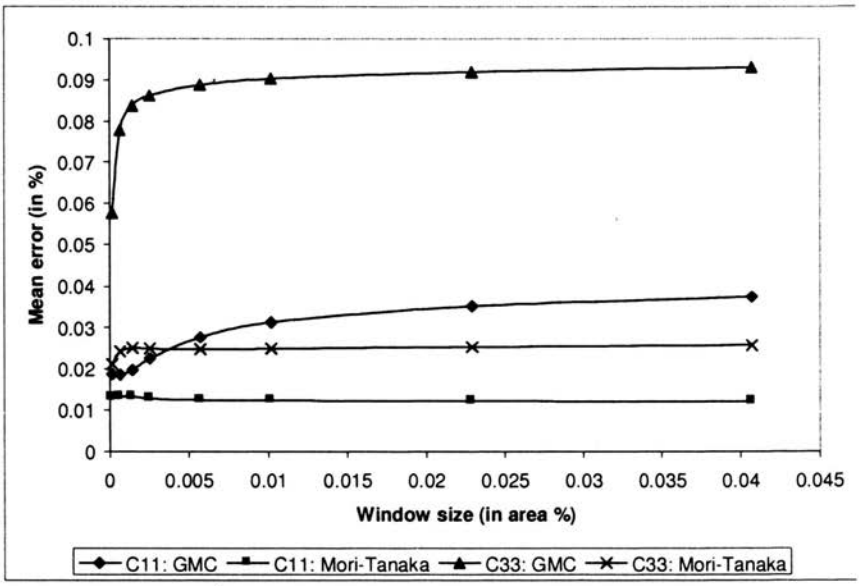

(b)

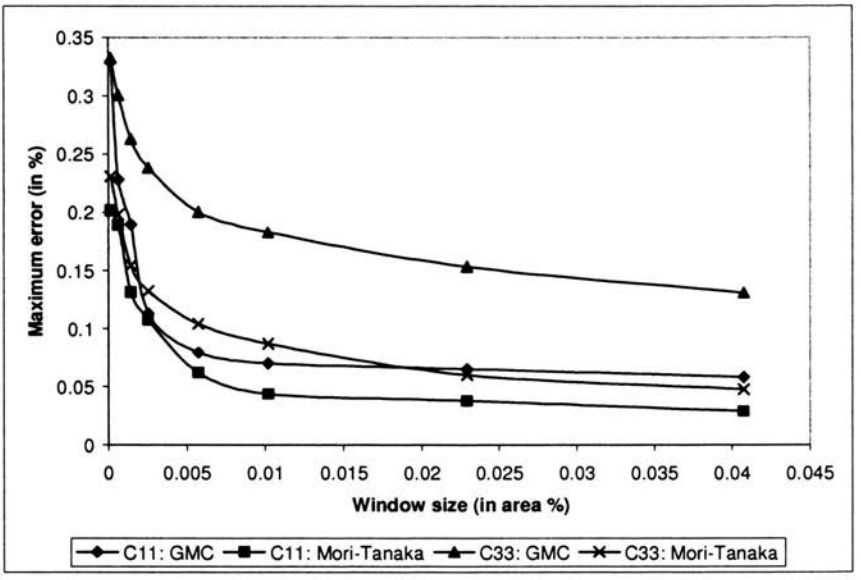

FIGURE 9. (a) Mean error relative to brute-force finite element results, for C_{11} and C_{33} obtained from GMC and Mori–Tanaka method. (b) Maximum error relative to brute-force finite element results, for C_{11} and C_{33} obtained from GMC and Mori–Tanaka method.

were compared with respect to the mean and maximum values of the stiffness elements $C_{11}(x_1, x_2)$ and $C_{33}(x_1, x_2)$, and are presented in Fig. 9, for varying window sizes.

The FE model was used as base line, since it did not initially depend on window size, and it does include shear-normal coupling. The error in the mean value of in $C_{11}(x_1, x_2)$ and $C_{33}(x_1, x_2)$ increases slightly with increasing window size. On average, these errors are small, $< 4\%$ for $C_{11}(x_1, x_2)$, and $< 9\%$ for $C_{33}(x_1, x_2)$. Errors in the maximum values, which exist at single points, are large by comparison and are again larger for the shear element, $C_{33}(x_1, x_2)$, than for the normal element, $C_{11}(x_1, x_2)$. In spite of the fact that the Mori–Tanaka model more strictly limits the degree of anisotropy and does not include the effects of the spatial arrangement of the phases, Mori–Tanaka shows less error than GMC for this heterogeneous microstructure.

Material anisotropy

The clustering of the microstructure introduces a second length scale within the microstructure which corresponds to the size of the clusters, (in addition to the size of the fibers). Because of this, the degree of local anisotropy may be influenced by both the spatial relationship of the fibers as well as the appearance of clusters against a random background. To investigate this effect, a second microstructure, similar in design, but without clusters, was also analyzed with respect to this ratio (see Fig. 10). In order to provide some quantification of the relative clustering of the two microstructures average cluster sizes were calculated for each of these microstructures.

If it is assumed that fibers spaced less than one-half of a fiber radius apart are part of the same cluster, then the average number of fibers per cluster in the clustered microstructure is 2.3, compared to 1.1 for the unclustered microstructure of 1.1, i.e., a ratio of 2:1 between the two microstructures.

With respect to the degree of local anisotropy, the mean value of the ratio C_{13}/C_{11}, which is identically zero for MT and GMC, is shown for the FE model in Fig. 10, for the clustered and unclustered microstructures.

As measured by this ratio, the degree of local anisotropy in both microstructures, as predicted by the finite element analysis, is extremely small. The unclustered microstructure generally shows a higher degree of anisotropy than does the clustered microstructure.

A comparison of the errors shown in Fig. 9, and the magnitude of the effects due to local anisotropy, as shown in Fig. 10, suggests that the micromechanical model and assumptions of material symmetry inherent in Mori–Tanaka and GMC are less significant than errors due to the isolated analysis of individual windows.

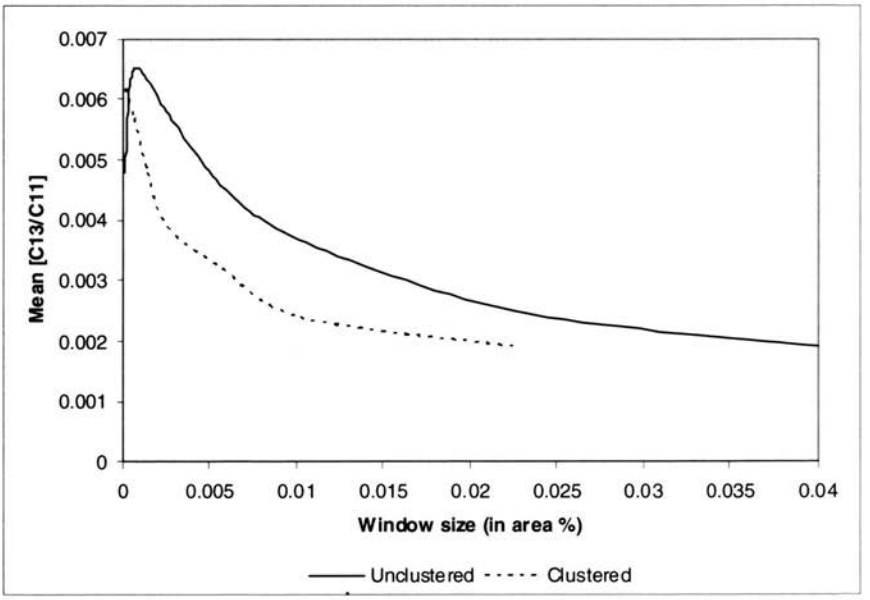

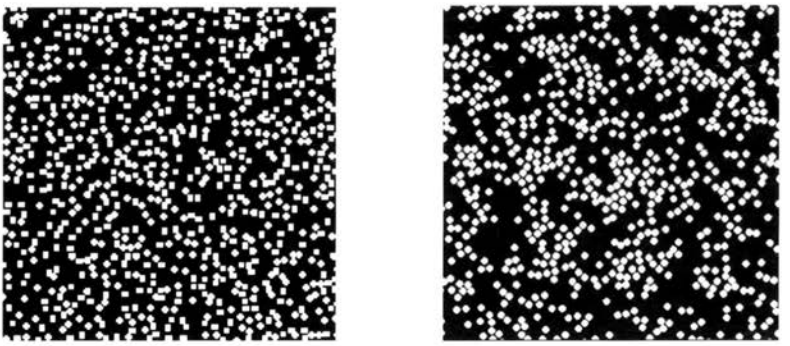

Unclustered Clustered

FIGURE 10. Mean ratio between C_{13} and C_{11} from FEA as a function of window size.

Correlation area

Perhaps the most useful measure for characterizing the effect of window size on the resulting material property field is sample correlation area. Correlation area is the two-dimensional extension of the correlation distance, or scale of fluctuation, for one-dimensional processes. It is loosely described as a measure of the maximum area over which material properties at different points are correlated.

Three methods were used to calculate the correlation area for each model:

1. the method based on the sample correlation function,
2. the method based on the sample spectral density function, and
3. the method based on the sample variance function (Vanmarcke, 1983).

Each of these techniques results in a range of possible values of the correlation area. By comparing the resulting ranges from all three techniques, an appropriate value for the sample correlation area was identified.

The correlation area is estimated in the first method by performing a discrete integration (a summation) of the sample correlation function:

$$\tilde{\alpha}_1 = \sum_{j=-N_{x_1}}^{N_{x_1}} \sum_{k=-N_{x_1}}^{N_{x_1}} \frac{\hat{B}_C(j\Delta x_1, k\Delta x_2)}{\hat{\sigma}_C^2} \Delta x_1 \, \Delta x_2. \tag{3.21}$$

The second method involves summation of the values of the spectral density function close to the wave numbers $\kappa_1, \kappa_2 = 0$,

$$\tilde{\alpha}_2 = \frac{\pi^2}{m^2 \hat{\sigma}_C^2} \sum_{\substack{j=-m \\ (j\neq 0)}}^{m} \sum_{\substack{k=-m \\ (k\neq 0)}}^{m} \frac{\hat{S}_C(\kappa_1, \kappa_2)}{\hat{\sigma}_C^2}. \tag{3.22}$$

The third method is based on the variance function and is generated by calculating a moving average of the sample material property field with window size A, defined by Vanmarcke (1983),

$$\tilde{\gamma}(A) = \frac{\hat{\sigma}_A^2}{\hat{\sigma}_C^2}, \qquad \tilde{\alpha}_3 = \frac{\tilde{\gamma}(A) A}{1 - \tilde{\gamma}(A)}. \tag{3.23}$$

In the above,

$$\hat{B}_C(j\Delta x_1, k\Delta x_2) = \frac{1}{N_{x_1} N_{x_2} - 1} \left[\sum_{m=1}^{N_{x_1}-j} \sum_{n=1}^{N_{x_2}-k} C(x_1^{(m)}, x_2^{(n)}) \, C(x_1^{(m+j)}, x_2^{(n+k)}) \right.$$
$$\left. - \left(\sum_{m=1}^{N_{x_1}} \sum_{n=1}^{N_{x_2}} C(x_1^{(m)}, x_2^{(n)}) \right)^2 \right], \quad j = 0, 1, \ldots N_{x_1} - 1, \quad k = 0, 1, \ldots N_{x_2} - 1, \tag{3.24}$$

is the sample correlation function with N_{x_1}, N_{x_2} the number of points and

$$\hat{\sigma}_C^2 = \frac{\left[\sum_{i=1}^{N_{x_1}} \sum_{j=1}^{N_{x_2}} C(x_1^{(i)}, x_2^{(j)})^2 - \left(\sum_{i=1}^{N_{x_1}} \sum_{j=1}^{N_{x_2}} C(x_1^{(i)}, x_2^{(j)}) \right)^2 \right]}{N_{x_1} N_{x_2} - 1} \tag{3.25}$$

is the sample variance.

$$\hat{S}_C(\kappa_1,\kappa_2) = \frac{1}{N_{x_1}N_{x_2}\Delta x_1\Delta x_2}\,|\Delta x_1\,\Delta x_2|\left[\sum_{m=1}^{N_{x_1}-1}\sum_{n=1}^{N_{x_2}-1} C(x_1^{(m)},x_2^{(n)}) \cdot \exp\left[-2i\pi\kappa_1^{(j)}\Delta x_1 m - 2i\pi\kappa_2^{(k)}\Delta x_2 n\right]\right] \tag{3.26}$$

is the sample spectral density function (Bendat and Piersol, 1986) using

$$\begin{aligned} &\kappa_1^{(j)} = \frac{j}{N_{x_1}\Delta x_1}, \qquad \kappa_2^{(k)} = \frac{k}{N_{x_2}\Delta x_2}, \\ &j = -N_{x_1}/2,\ldots,-1,0,1,\ldots,-N_{x_1}/2, \\ &k = -N_{x_2}/2,\ldots,-1,0,1,\ldots,-N_{x_2}/2, \end{aligned} \tag{3.27}$$

which are values in the 2-dimensional wave domain.

For the sample, an average value, $\tilde{\alpha}$, which satisfied the ranges of all three formulas was used. Figure 11 plots the results using MW-GMC, but the results for the other models were virtually identical because the material property fields were almost identical.

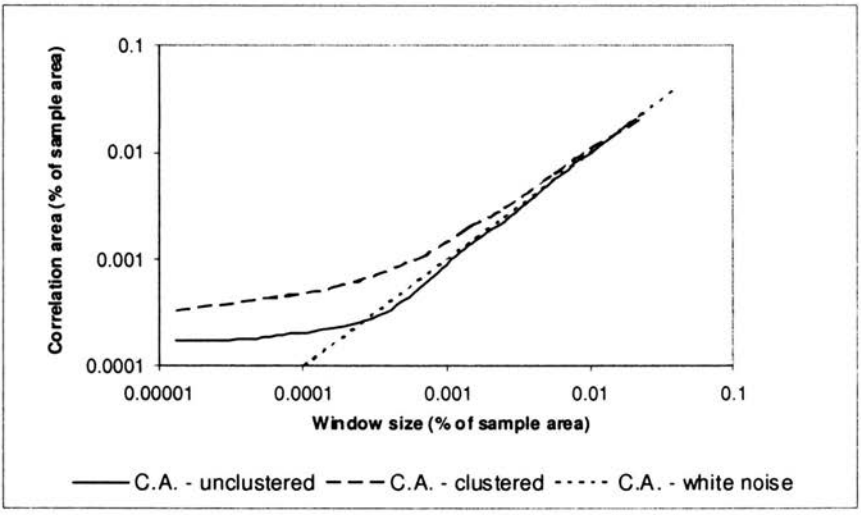

FIGURE 11. Correlation area for the clustered sample, unclustered sample and white noise process.

For comparsion the correlation areas for both the clustered and unclustered samples, as well as a plot of the line representing a linear relationship,

between window size and correlations area, white noise, are included on the graph.

It is clear from Fig. 11 that for large windows the moving-window results reflect so much smoothing that only the local average of a white noise process is recovered. In other words, when the window size is too large all information about the microstructure is lost through excessive smoothing of the field.

This suggests that a criterion for an upper bound on the window size could be the smallest window size at which this trend begins, i.e., the smallest window dimension for which the correlation area is approximately equal to the window size. The results from the clustered microstructure suggest that the moving windows applied to this microstructure should be no larger than 120 pixels square, (full size 275×275) or 0.16% of the sample area. The results from the unclustered microstructure suggest a much tighter constraint in that the window should be no larger than approximately 30 pixels square, or 0.04% of the sample area. Note that the window size for the unclustered microstructure of 30 pixels square corresponds to slightly larger than one fiber size, and the window size for the clustered microstructure of 120 pixels corresponds approximately to the average cluster size. This suggests that the analysis of a clustered microstructure allows larger windows than does that for an unclustered microstructure, due to the larger length-scale of the clusters of inclusions. The choice would then depend on whether the influence of the clustering was the more significant.

3.4.2. Window size revisited. In the previous section, the correlation area analysis suggested a criterion for the largest window size that should be used for a given microstructure. The next goal would be to find an estimate for the smallest size that would be appropriate. The smallest windowing scheme is obviously the original digital field, where each pixel is associated with one material and its properties. For the ultimate statistical and simulation purposes this level of smoothing is unacceptable due to the computational difficulties associated with the noise in these fields. To illustrate the extremes, the solution of a single circular inclusion under a uniform far-field stress was considered. The boundary conditions for this problem are

$$\begin{aligned} \sigma_{11}(x_1, x_2 = \pm\infty) &= 0, \\ \sigma_{22}(x_1, x_2 = \pm\infty) &= 1, \\ \sigma_{12}(x_1, x_2 = \pm\infty) &= 0. \end{aligned} \tag{3.28}$$

Traction and displacement continuity conditions were enforced across the fiber/matrix interface. The reason for selecting this particular configuration

is that an analytical solution for the stress distribution in the fiber and matrix can be found Timoshenko and Goodier (1951), so that a direct comparison of results from a moving-window analysis to the known elasticity solution can be made.

In order to perform a moving-window analysis of the single fiber problem, digitized images of the circular fiber were constructed using a range of resolutions. As an approximation to the infinite matrix surrounding the fiber, the image size was made approximately 25 times that of the fiber size. In other words, the fiber radius was maintained at one-tenth the length of each side of a square sample. Increasing levels of resolution/magnification of the inclusion were represented by an increasing number of pixels, as shown in Fig. 12. For each of these digitized images, property fields were calculated using the moving-window technique with GMC. Window sizes ranged from 1 pixel, which is the unsmoothed field, to the total number of pixels in the discretized image, which produced a single value for the field, that of the effective property.

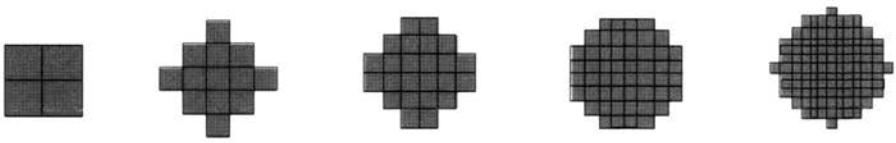

FIGURE 12. Varying resolution of fibers- discretization with pixels. Surrounding matrix was discretized using the same size pixels.

When the smallest possible window size was used (1 pixel), then there was no smoothing of the elastic properties and the elastic moduli were assigned according to each pixel (Fig. 13(a)). When this unsmoothed data was used as input in a finite element code, with one element equal to one pixel, the maximum stress results in stress concentrations appearing at the corners of the squared edges of the inclusion (see Fig. 13(b)). Of course, this effect will occur regardless of the level of resolution, since the digitization process is forced to approximate a circular boundary using rectangular pixels, however, as the window size increases, the level of discontinuity between the elastic properties at adjacent finite elements will decrease. This effect will be visible in the finite element results as a reduction in the magnitude of the stress concentrations that occur as a result of the digitization process.

Assuming that the elastic modulus of the inclusion material is twice that of the matrix material, the stress distribution in the far-field stress problem was estimated by applying moving-window GMC property fields to a finite element analysis of the sample under uniaxial tension. The local transverse

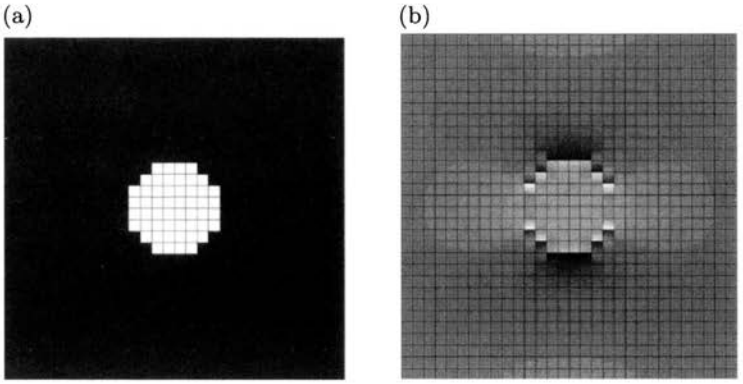

FIGURE 13. (a) Field of elastic modulus E_{22}. (b) Corresponding stress field σ_{22} from finite element modeling. Light shades are higher values. Elastic modulus of fiber is twice that of matrix. Window size one pixels. High stresses localized at corners of fiber.

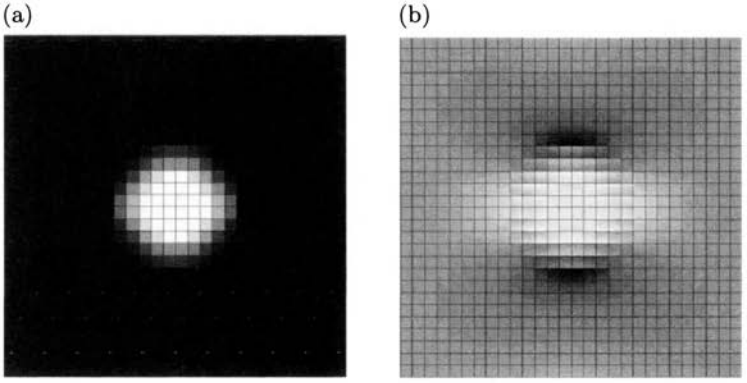

FIGURE 14. (a) Field of elastic modulus E_{22} (b) Corresponding stress field σ_{22} from finite element modeling. Light shades are higher values. Elastic modulus of fiber is twice that of matrix. Window size three pixels. High stresses at corners of fiber muted.

elastic modulus fields $E_{22}(x_1, x_2)$, as well as the corresponding stress fields $\sigma_{22}(x_1, x_2)$, for the 30×30 pixel resolution, developed from two window sizes, 1 and 3 pixels, are shown in Figs. 13(a-b) and 14(a-b).

In Fig. 15 the maximum stress, σ_{22}, is given for each of the 5 resolutions illustrated in Fig. 12, as a function of window size. The solution for the maximum value $\sigma_{22} = 1.27$, obtained from the elasticity solution, is plotted as the horizontal line on the same graph. In order to evaluate the effect of an increased contrast ratio between the elastic moduli of the fiber and matrix,

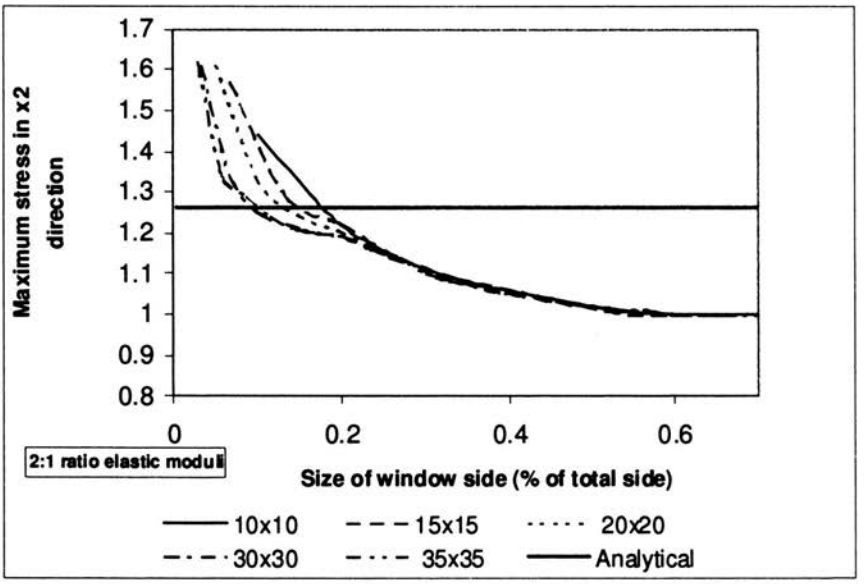

FIGURE 15. Maximum transverse stress in composite with 2:1 ratio of fiber modulus to matrix modulus, 5 resolutions, varying window sizes, compared to analytic solution.

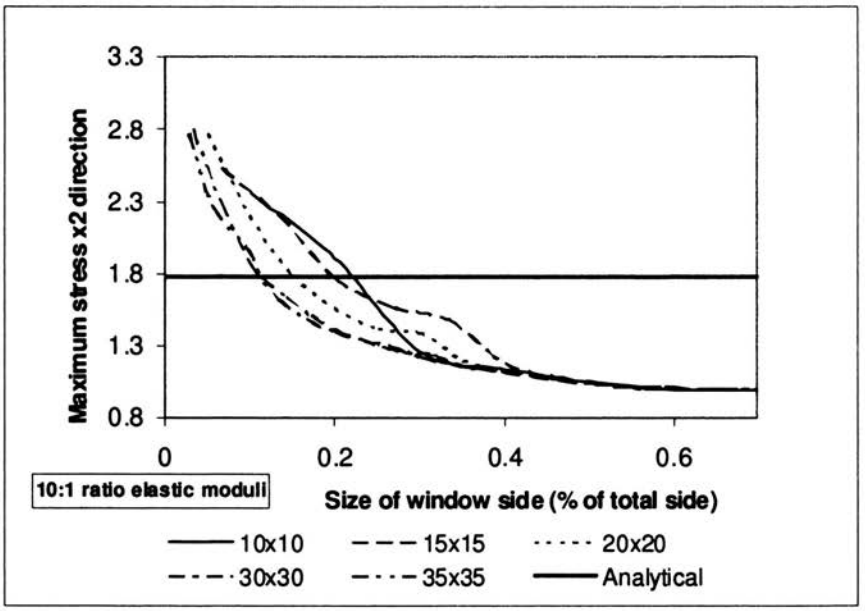

FIGURE 16. Maximum transverse stress in composite with 10:1 ratio of fiber modulus to matrix modulus, 5 resolutions, varying window sizes, compared to analytic solution.

the maximum local stresses were also calculated for a contrast ratio of 10:1 and are presented in Fig. 16. The elasticity solution for this case, $\sigma_{22} = 1.78$ is again plotted as a horizontal line on this graph. Both of these figures suggest that "too small" a window yields unrealistically high estimates of the maximum stress, an effect that increases with higher contrast ratios. If the window is "too large" though, the material properties are homogenized, and the stresses throughout the inclusion and the matrix are constant.

When compared to the analytic solution, these results suggest that an appropriate range of window sizes is from approximately 15% × 15% to approximately 25%×25% of the sample size, or roughly the size of the inclusion, which has a diameter equal to 20% of the sample size. This result appears to be consistent for both the low and high contrast ratio.

The physical model of a single fiber in an infinite matrix is the extreme of an unclustered microstructure. The results from the previous section on correlation areas, suggest that as clustering of inclusions is introduced the maximum allowable window size may be increased. The results from this section suggest that the size of a single fiber may prove to be a reasonable estimate for the lower bound on window size.

Based on these guidelines, the range of window size should be somewhere between the size of one fiber area and the average size of the cluster, for the clustered microstructure. For the unclustered microstructure the minimum and maximum window size form a narrow range about the size of the fiber.

4. Experimental validation and verification

Most of the experimental methods capable of producing field information rely on optical data. These include photoelasticity, moiré and shadow moiré, holography and speckle interferometry, heterodyning and gradient sensing, interferometry, moiré interferometry and thermography, (Knauss, 2000). The information is generally in the form of fringe patterns and spatial resolution is on the order of a millimetre. Interferometry and moiré interferometry can resolve displacements to smaller scale, to approximately the wavelength of light, $\sim$ 1 micron, and can potentially offer finer resolutions "... when used carefully" (Knauss, 2000). The applications of moiré interferometry range from modelling fiber/matrix deformation in metal matrix composites (Han 1992), measuring/monitoring corrosion (Huang et al., 1999), to the microstructural analysis of biological materials (Gaudette et al, 1999).

Digital Image Correlation (DIC) is a relatively new technique, by comparison, having most recently come into its own with the speed and easy availability of high-speed computers (Sutton et al, 1983, Chu et al, 1985, Sutton et al. 1986, Sutton et al. 1988). The method is well suited to investi-

gations at extremely small scales, at the range of micro- or nanomechanics, first because DIC allows simultaneous determination of displacements and gradients and second because visual tools such as SEMs, TEMs, (scanning and electron microscopes) and STMs and ATMs, (scanning tunnelling and atomic force microscope) yield digital images.

DIC is a computer-based, optical measurement technique proven to be accurate and efficient for obtaining full-field surface displacements, and displacement gradients (Sutton et al, 2000a, 2000b). Assuming a continuous (affine) transformation (Vendroux and Knauss, 1998) between undeformed and deformed images, local strains are determined by minimization of a correlation function between the undeformed and the deformed states. In order to affect the matching process, the surface of the object must have a random (non-repeating) pattern (e.g., speckle pattern), which produces varying photographic (light) intensities in a digital image; in other words it produces an image in which the pattern is visible because of different gray-scale levels associated with individual pixels. This pattern can either be inherent to the surface or one that is applied. Suitable patterns have been applied using sprayed droplets of paint, particles of printing toner, and pattern imprinting via a template and photolithography. Microstructural features are also possible as pattern elements.

In the next phase of the moving window project we propose to use DIC to provide an experimentally defined basis for evaluating and modifying the computational moving-window analyses. The choice of DIC for this work is based on two main considerations. Primarily the appeal of this method is that the basis of DIC is a digital image and displacements are developed by statistical matching (correlation) and averaging over a micro-length scale (subset of the full image). The Moving Window Micromechanics technique is very similarly constructed, using a digital image and smoothing over a window (subset of the full image). Thus, it is reasonable to expect that results from the two methods could be effectively linked and correlated. Second, the potential ability of the DIC method to extend to smaller length scales expands the range of material systems that can be employed in this and future studies.

4.1. How image correlation works

Numeric values of gray scale intensities corresponding to the pattern of microstructural elements or to an applied pattern can be read off a digitized image. Ideally, the numbers form patterns matching the physical pattern. When the material is deformed, the image deforms and there is a corresponding shift in the numeric pattern of the gray scales.

The idea behind image correlation is to compare the undeformed image to the deformed image and match up how the pattern has shifted and distorted. If a pixel can be tracked from its original position to a deformed position then the displacement can be measured and strains calculated. Figure 17 shows a digitized pattern and idealized intensities associated with the pattern. Figure 18 shows the same pattern after deformation.

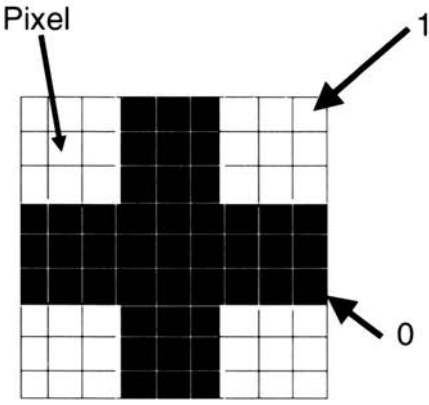

100	100	100	0	0	0	100	100	100
100	100	100	0	0	0	100	100	100
100	100	100	0	0	0	100	100	100
0	0	0	0	0	0	0	0	0
0	0	0	0	0	0	0	0	0
0	0	0	0	0	0	0	0	0
100	100	100	0	0	0	100	100	100
100	100	100	0	0	0	100	100	100
100	100	100	0	0	0	100	100	100

FIGURE 17. Idealized undeformed image, pixel grey scales correspond to pattern elements registering either 0 or 100 in intensity.

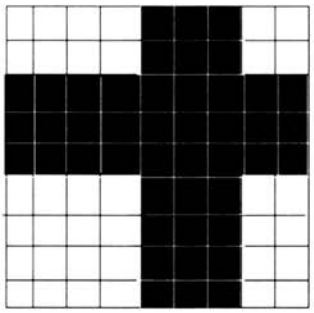

100	100	100	100	0	0	0	100	100
100	100	100	100	0	0	0	100	100
0	0	0	0	0	0	0	0	0
0	0	0	0	0	0	0	0	0
0	0	0	0	0	0	0	0	0
100	100	100	100	0	0	0	100	100
100	100	100	100	0	0	0	100	100
100	100	100	100	0	0	0	100	100
100	100	100	100	0	0	0	100	100

FIGURE 18. Idealized deformed image, pixel grey scales correspond to pattern elements registering either 0 or 100 in intensity.

While it is fairly easy to track the deformation between these two images and map pixels from Fig. 17 to Fig. 18, for larger images, more detailed patterns and more complex deformations, a method of automating this matching process is obviously required. This can be done by selecting a sequence of small subsets of the original image and calculating a cross correlation function between each of these areas and all possible similarly sized areas in the

deformed image. The region with the minimum correlation value corresponds to the deformed location of the original subset. The correlation function is given in Eq. (4.1).

$$C(x,y,u,v) = \sum_{i,j=-n/2}^{n/2} (I(x+i,y+j) - I^*(x+u+i,y+v+j))^2. \quad (4.1)$$

In Eq. (4.1), I, is the numeric value of the intensity of the undeformed image at each pixel location, done here at integer locations. I^* is the intensity in the deformed image. The variables x and y correspond to the location of the pixel, and the variables u and v are the displacements of the comparing subset area in the x and y directions. Performing this calculation on the sample shown in Figs. 17 and 18, might lead to a comparison of the two subsets shown in Fig. 19.

In the case of Fig. 19, the correlation function for the 5×5 subset centered at pixel ($x = 5$, $y = 5$) is given by

$$C(5,5,-2,-2) = \sum_{i,j=-2}^{2} \left(I(5+i,5+j) - I^*(5-2+i,5-2+j)\right)^2, \quad (4.2)$$

where the (-2)'s correspond to the relative position (the center point) of the subset to which the undeformed region is being compared. Expanding this out yields

$$\begin{aligned}
&(100-0)^2 + (0-0)^2 + (0-0)^2 + (0-0)^2 + (100-0)^2 \\
&+ (0-100)^2 + (0-100)^2 + (0-100)^2 + (0-100)^2 + (0-0)^2 \\
&+ (0-100)^2 + (0-100)^2 + (0-100)^2 + (0-100)^2 + (0-0)^2 \\
&+ (0-100)^2 + (0-100)^2 + (0-100)^2 + (0-100)^2 + (0-0)^2 \\
&+ (100-100)^2 + (0-100)^2 + (0-100)^2 + (0-100)^2 \\
&+ (100-0)^2 = 18\,000.
\end{aligned} \quad (4.3)$$

Since it is possible to find the deformed position in this example by inspection it is not surprising that this subset's correlation value is high. In this idealized example, the correlation function for the real deformed position of this subset is exactly zero (see Fig. 20). Zero being the absolute minimum for a sum of squared numbers.

In real life, the numbers are not as clean and exact. A more realistic example might be more like the one shown in Fig. 21, where, although it is still possible to visually track the deformation using the grids shown, the

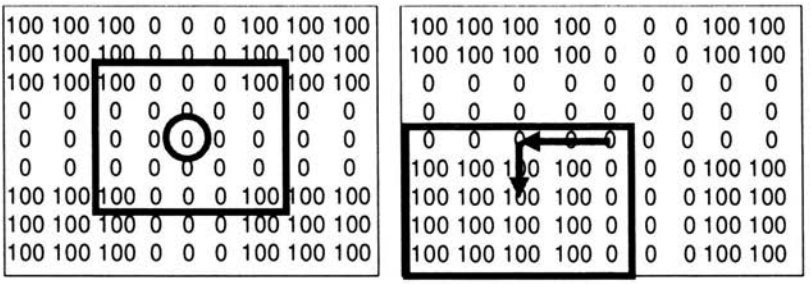

FIGURE 19. Image analysis compares correlation function values of subsets in deformed image to find match in undeformed image. The undeformed subset (with circled center) is compared to an arbitrary subset in deformed image. Arbitrary deformed area is shifted 2 to the left and 2 down from the circled center point of the undeformed subset.

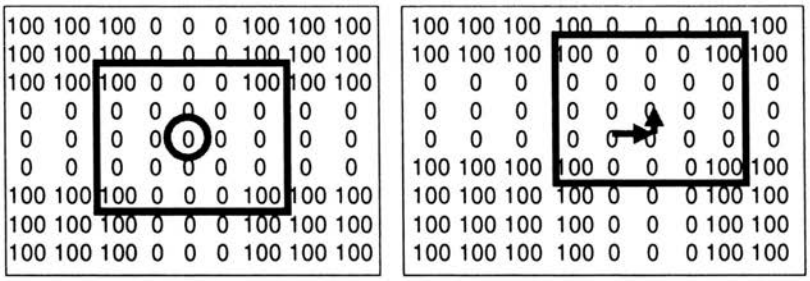

FIGURE 20. Image analysis compares correlation function of subsets in deformed image to find match in undeformed image. Subset with minimum correlation function value, $C(5, 5, 1, 1) = 0$.

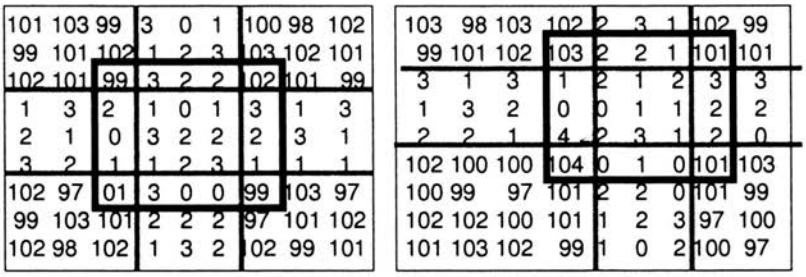

FIGURE 21. Image analysis compares subsets between undeformed and deformed images to find match in undeformed image. Intensities illustrated here include signal noise.

correlation function value for the match is no longer identically zero.

$$\begin{aligned} C(5,5,1,1) = {} & (99-103)^2 + (3-2)^2 + (2-2)^2 + (2-1)^2 \\ & + (102-101)^2 + (2-1)^2 + (1-2)^2 + (0-1)^2 \\ & + (1-2)^2 + (3-3)^2 + (0-0)^2 + (3-0)^2 + (2-1)^2 \\ & + (2-1)^2 + (2-1)^2 + (1-4)^2 + (1-2)^2 + (2-3)^2 \\ & + (3-1)^2 + (1-2)^2 + (101-104)^2 + (3-0)^2 \\ & + (0-1)^2 + (0-0)^2 + (99-101)^2 = 71. \end{aligned} \tag{4.4}$$

The positions of points in the original image will usually map to non-integer values in the deformed subset, so sub-pixel accuracy is achieved by interpolation. It is assumed that the gray level of each pixel of the deformed image is the value at the pixel's center and that values of the gray levels off center can be determined using bi-cubic interpolation. It has been shown that accuracies in displacements of 0.002 pixels can be achieved using this method. Minimization of the cross-correlation function with respect to its six variables is done using a Levenberg–Marquardt algorithm. This algorithm combines a Newton–Raphson root-finding approach with the Method of Steepest Descent, (Helm et al., 1996). Programs implementing these methods have been developed and are capable of determining displacements at over 5 000 points per second using standard PC computers. The correlation program determines displacements that can be converted to strains using surface fits to the displacement fields. This method typically will produce strain-fields with accuracy of 100 μ-strain.

4.2. Application: Large scale composite

In order to test the feasibility of using DIC to verify the Moving Window Methodology, an artificial composite sample was fabricated. The composite consists of a resin epoxy matrix and wooden, toothpicks and dowels, $\sim$ "fibres". The idea behind fabricating at this large scale was to end up with a composite that could be tested in existing large scale testing apparatus, with an easily visible microstructure that could be used as the correlation pattern without requiring magnification. Figure 22 shows some of the fabricated samples.

4.2.1. Image correlation of the fabricated composite. Tension testing was performed on a sample with displacement control. Images were at a strain rate of $5 \cdot 10^{-4}$. Using the digital image correlation software VIC-2D, developed at the University of South Carolina (marketed by Correlated Solu-

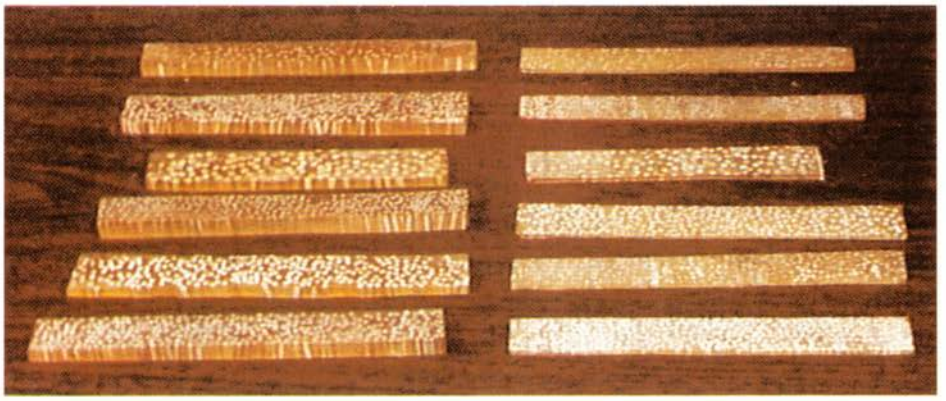

FIGURE 22. Transverse sections of large scale resin-wood composites.

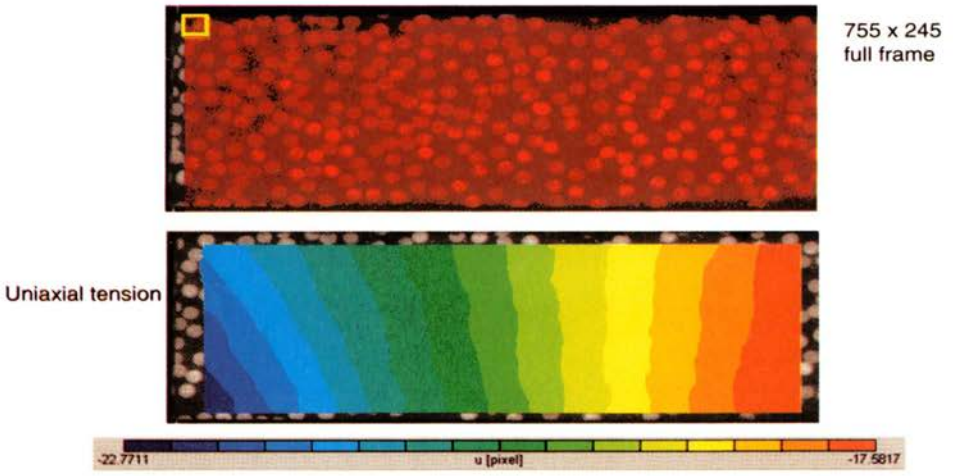

FIGURE 23. (Top:) Area of interest and subset (29 pixels square) overlaid on image of undeformed sample. (Bottom:) Horizontal (u) displacement in tension. Grip to left moves, grip at right is stationary. Range: $u \in [-22.77, -17.58]$.

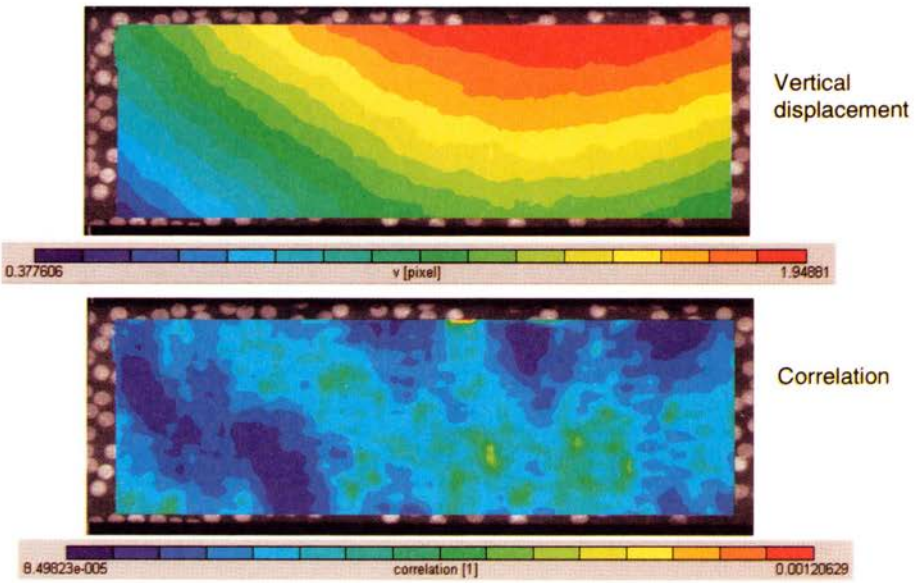

FIGURE 24. (Top:) Vertical (v) displacement in tension. (Bottom:) Correlation function values. Range: $v \in [0.378, 1.95]$, error $\in [8.5 \cdot 10^{-5}, 1.2 \cdot 10^{-4}]$.

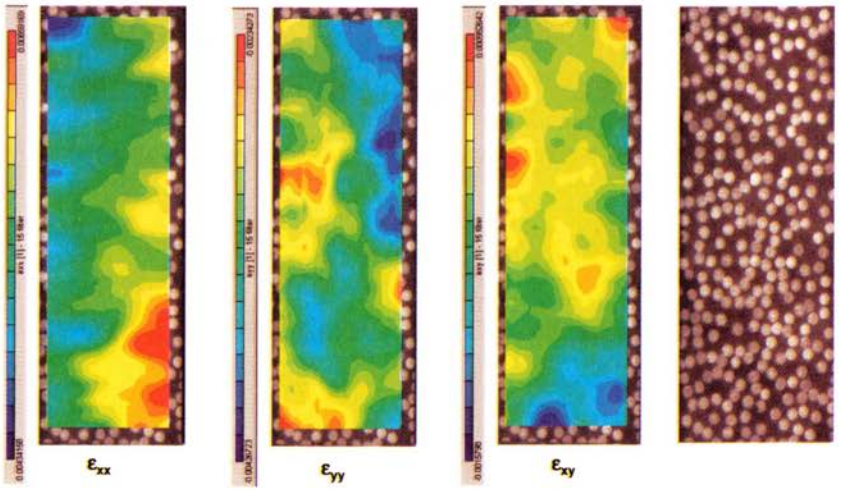

FIGURE 25. Strain fields approximated using VIC-2D software: axial, transverse and shear. Loading is in the x-direction (up in these images). Microstructure is shown for comparison.

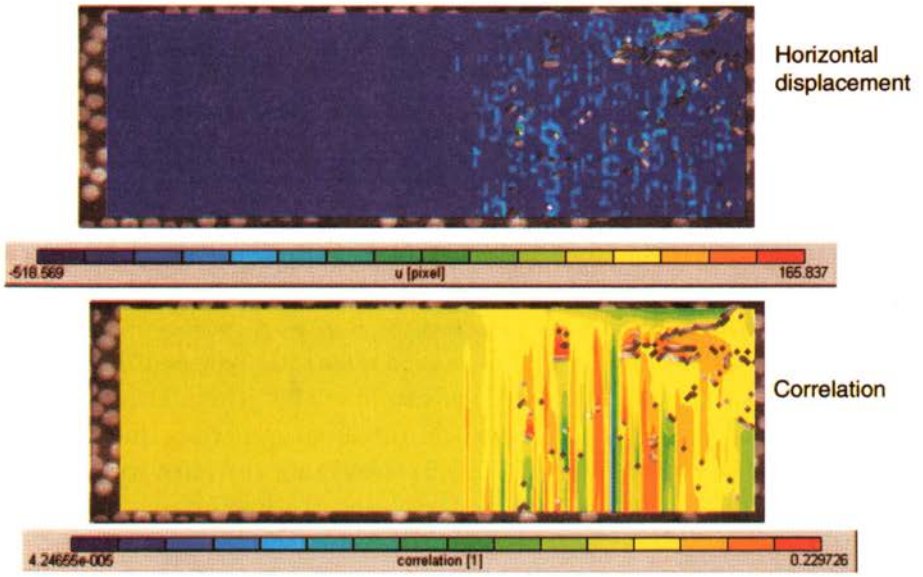

FIGURE 26. Subset size 9 pixels^2. (Top:) Horizontal (u) displacement in tension. (Bottom:) correlation – errors.

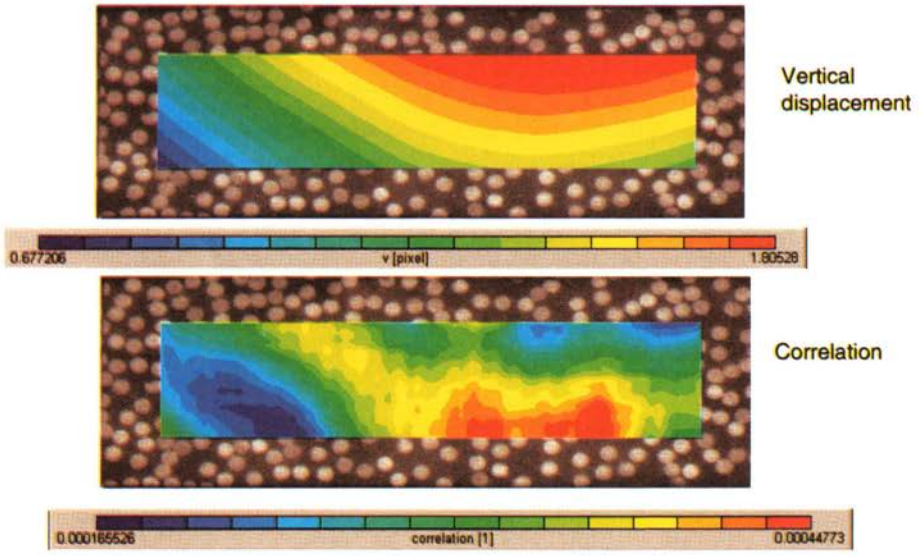

FIGURE 27. Subset size 101 pixels^2. (Top:) Vertical (v) displacement in tension. (Bottom:) Correlation function values. Range: $v \in [0.68, 1.8]$, error $\in$ [0.00017, 0.00045].

tions `http://www.correlatedsolutions.com/`) correlation was done on the deformed images.

Figure 23 (top) shows the area of interest and subset used in correlation. The subset is 29 x 29 pixels, approximately the size of two pattern elements (fibres). Theoretically an image resulting from uniaxial tension will show vertical bands, perpendicular to the loading direction. The bottom image in Fig. 23, the horizontal displacement (pixels) shows a reasonably clean deformation away from the grips. The tilting of the displacement bands near the right end suggests either some slipping in the grips or the presence of some other edge effect.

The image at the top of Fig. 24, which shows the vertical displacement transverse to the loading, shows some bending; this is due either to failure in even gripping or to the differences in material properties due to the microstructure. The bottom image of Fig. 24 shows that the software was able to accurately correlate the images based on using the microstructural features as pattern elements.

The strains calculated by VIC-2D are shown in Fig. 25.

When a smaller subset size (9) is used, the subset can fit between the pattern elements and cannot correlated that region. Figure 26 shows the attempt to correlate the horizontal displacement (note large pixel displacement values) and the larger values for correlation, suggesting errors.

A larger subset size (101×101) produces smoother fields; small correlation values suggest low error. Note that the size of the subset limits the resulting field of data. The next stage of the project is to develop material property fields of the same sample using a variety of window sizes, use the fields as input into a finite element model of uniaxial tension (plane strain) and compare the fields.

References

1. J. ABOUDI, *Mechanics of Composites: A Unified Micromechanical Approach*, Elsevier, Amsterdam, 1991.

2. S. NEMAT-NASSER and M. HORI, *Micromechanics: Overall Properties of Heterogeneous Materials*, 2nd Edition, Elsevier, 1999.

3. W. VOIGT, Über die Beziehung zwischen den beiden Elastizitätskonstanten isotroper Körper, *Wied. Ann. Physik*, Vol.38, pp.573-587, 1889.

4. A. REUSS, Berechnung der Fliessgrenze von Mischkristallen auf Grund der Plastizitätsbedingung für Einkristalle, *Z. Angew, Math. Mech.*, Vol.9, pp.49-58, 1929.

5. R. HILL, The elastic behavior of a crystalline aggregate, *Proc. Phys. Soc. London*, Vol.A65, pp.376-355.

6. Z. HASHIN, The elastic moduli of heterogeneous materials, *J. Appl. Mech.*, Vol.29, pp.143-150, 1962.

7. Z. HASHIN and S. SHTRIKMAN, A variational approach to the theory of the elastic behavior of multiphase materials, *J. Mech. Phys. Solids*, Vol.211, pp.127-140, 1963.

8. J.D. ESHELBY, The determination of the elastic field of an ellipsoidal inclusion and related problems, *Proc. Roy. Soc.*, Vol.A241, pp.376-396, 1957.

9. J.D. ESHELBY, The elastic field outside an ellipsoidal inclusion, *Proc. Roy. Soc.*, Vol.A252, pp.561-569, 1959.

10. J.D. ESHELBY, Elastic inclusions and inhomogeneities, in: *Prog. in Solid Mech.*, I.N. Sneddon and R. Hill (Eds.), North-Holland, Vol.II, pp 89-140, 1961.

11. T. MURA, *Micromechanics of Defects in Solids*, 2nd Edition, Matinus Nijhoff, Dordrecht, 1987.

12. A.V. HERSHEY, The elasticity of an isotropic aggregate of anisotropic cubic crystals, *J. Mech, Phys. Solids*, Vol.11, pp.127-, 1954.

13. E. KRÖNER, Berechnung der elastischen Konstanten des vielkristalls aus den Konstanten des Einkristalls, *Z. Phys.*, Vol.151, pp.504.

14. R. HILL, A self-consistent mechanics of composite materials, *J. Mech. Phys. of Solids*, Vol.13, pp.213-222, 1965.

15. B. BUDIANSKY, On the elastic moduli of some heterogeneous materials, *Mech. Phys. of Solids*, Vol.13, pp.223-227, 1965.

16. T. MORI and K. TANAKA, Average stress in matrix and average elastic energy of material with misfitting inclusions, *Acta Metall.*, Vol.21, pp.571-574, 1973.

17. Y. BENVENISTE, A new approach to the application of Mori–Tanaka's theory in composite materials, *Mechanics of Materials*, Vol.6, pp.147-157, 1987.

18. C. HERAKOVICH, *Mechanics of Fibrous Composites*, John Wiley and Sons, New York, 1998.

19. K. SOBCZYK and D. KIRKNER, *Stochastic Modeling of Microstructures*, Birkhäuser, Boston, 2001.

20. S. TORQUATO, *Random Heterogeneous Materials: Microstructure and Macroscopic Properties*, Springer-Verlag, New York, Inc. 2002.

21. M. BERAN and J. MOLYNEUX, Use of classical variational principles to determine bounds for the effective bulk modulus in heterogeneous media, *Quart. Appl. Math.*, Vol.24, No.2, pp.107-118, 1966.

22. J.A. QUIBLER, A new three-dimensional modeling technique for studying porous media, *J. Colloidal Interface Sci.* Vol.98, pp.84-102, 1984.

23. P.M. ADLER, C.G. JACQUIN, and J.A. QUIBLER, Flow in simulated porous media, *Int. J. Multiphase Flow*, Vol.16. pp 691-712, 1990.

24. C. MANWART, S. TORQUATO, and R. HILFER, Stochastic reconstruction of sandstones, *Physical Review E*, Vol.62, No.1 pp.893-899, 2000.

25. M.D. RINTOUL and S. TORQUATO, Reconstruction of the structure of dispersions, *J. Colloidal Interface Sci.*, Vol.186, pp 467-476, 1997.

26. A.P. ROBERTS and M.A. KNACKSTEDT, Structure-property correlations in model composite materials, *Physical Review E*, Vol.54, No.3, pp.2313-2328, 1996.

27. A.P. ROBERTS and E.J. GARBOCZI, Computation of the linear elastic properties of random porous materials with a wide variety of microstructure, *Proc. Roy. Soc. Series A*, Vol.458, No.2021, pp 1033-1054, 2002.

28. A.P. ROBERTS and M. TEUBNER, Transport properties of heterogeneous materials derived from gaussian random fields: Bounds and simulations, *Phys. Rev. E*, Vol.51, No.5, pp.4141-4154, 1995

29. S. TORQUATO, Random heterogeneous media: microstructure and improved bounds on effective properties, *Appl. Mech. Rev.*, Vol.44, pp.37-76, 1991.

30. G.L. POVIRK, Incorporation of microstructural information into models of two-phase materials, *Acta Metallurgica et Materialia*, Vol.43, pp.3199-3206, 1995.

31. S.C. BAXTER and L.L GRAHAM, Characterization of random composites using a Moving Window Technique, *ASCE Journal of Engineering Mechanics*, Vol.126, No.4, pp.389-404, 2000.

32. L.L. GRAHAM and S.C. BAXTER, Stochastic finite element analysis of composite structures with random imperfections, in: *Stochastic Structural Dynamics*, B.F. Spencer, Jr. and E.A. Johnson (Eds.), University of Notre Dame, Balkema, Rotterdam, pp.159-164, 1998.

33. B. LU and S. TORQUATO, Local volume fraction fluctuations in heterogeneous media, *J. Chem. Phys.*, Vol.93, No.5, pp.3452-3459, 1990.

34. M. OSTOJA-STARZEWSKI, Micromechanics as a basis of continuum random fields, *Applied Mechanics Reviews*, Vol.47, No.1, pp.S221-S230, 1994.

35. M. OSTOJA-STARZEWSKI and X. WANG, Stochastic finite elements as a bridge between random material microstructure and global response, *Comput. Methods Appl. Mech. Engrg.*, Vol.168, pp.35-49, 1999.

36. W.H. TANG and R.B. GILBERT, Statistics of spatial average in a random two-state medium, *Structural Safety*, Vol.6, pp.271-282, 1989.

37. M. PALEY and J. ABOUDI, Micromechanical analysis of composites by the generalized cells model, *Mech. Mater.*, Vol.14 pp.127-139, 1992.

38. J. ABOUDI, Micromechanical analysis of composites by the method of cells, *Applied Mechanics Reviews*, ASME, Vol.42, pp.193-221, 1989.

39. L. GRAHAM-BRADY, E. SIRAGY, and S. BAXTER, Analysis of heterogeneous composites based on Moving Window Techniques, *J. Eng. Mech.*, Vol.129, No.9, pp.1054-1064.

40. E. VANMARCKE, *Random Fields*, MIT Press, 1983.

41. J.S. BENDAT and A.G. PIERSOL, *Random Data: Analysis and Measurement Procedures*, John Wiley & Sons. 1986.

42. S. TIMOSHENKO and J.N. GOODIER, *Theory of Elasticity*, McGraw-Hill, New York, 1951.

43. W.G. KNAUSS, Perspectives in experimental solid mechanics, *Inter. J. Solids Struc.*, Vol.37, pp.251-266, 2000.

44. B. HAN, Higher sensitivity moiré interferometry for micromechanics studies, *Optical Engineering*, Vol.31, No.7, pp.1517-1526, 1992.

45. P.S. HUANG, F. JIN, and F.P. CHIANG, Quantitative evaluation of corrosion by a digital fringe projection technique, *Optics and Lasers in Engineering*, Vol.31, No.5, pp.371-380, 1999.

46. G.R. GAUDETTE, F.P. CHIANG, J. TODARO, and I.B. KRUKENKAMP, A novel technique for measuring epicardial deformation with high spatial resolution, *Biophysical Journal*, Vol.76, No.1, pp.A309-A309, Part 2, 1999.

47. M.A. SUTTON, W.J. WOLTERS, W.H. PETERS, W.F. RANSON, and S.R. MCNEILL, Determination of displacements using an improved digital correlation method, *Image Vision, Computing*, Vol.1, No.3 pp.133-139, 1983.

48. T.C. CHU, W.F. RANSON, M.A. SUTTON, and W.H. PETERS, Applications of digital image correlation techniques to experimental mechanics, *Exper. Mech.*, Vol.25, No.3, pp.232-244, 1985.

49. M.A. SUTTON, M. CHENG, W.H. PETERS, Y.J. CHAO, and S.R. MCNEILL, Application of an optimized digital image correlation method to planar deformation analysis, *Image Vision Computing*, Vol.4, No.3, pp.143-150, 1986.

50. M.A. SUTTON, S.R. MCNEILL, J. JANG, and M. BABAI, The effect of subpixel image resaturation on digital image correlation estimates, *Optical Engineering*, Vol.27, No.10, pp.870-877, 1988.

51. M.A. SUTTON, S.R. MCNEILL, J.D. HELM, and Y.J. CHAO, Advances in two-dimensional and three-dimensional computer vision, in: *Photomechanics. Topics in Applied Physics*, P.K. Rastogi (Ed.), Springer-Verlag, Berlin Heidelberg, Vol.77, pp.323-372, 2000.

52. M.A. SUTTON, S.R. MCNEILL, J.D. HELM, and H.W. SCHREIER, Computer vision applied to shape and deformation measurement, in: *Trends in Optical Nondestructive Testing and Inspection*, P.K. Rastogi and D. Inaudi (Eds.), Elsevier Science B.V., 2000.

53. G. VENDROUX and W.G. KNAUSS, Submicron deformation field measurements – part 2: Improved digital image correlation, *Exper. Mech.*, Vol.38, No.2, pp.86-92, 1998.

54. J.D. HELM, S.R. MCNEILL, and M.A. SUTTON, Improved 3-D Image Correlation for Surface Displacement Measurement, *Opt. Eng.*, Vol.36, No.8, pp.2361-2361 1997.